DEVELOPMENT OF A MAGNETIC CONFINEMENT ATTACHMENT FOR ENHANCED SIGNAL IN HANDHELD LASER INDUCED BREAKDOWN SPECTROSCOPY SOIL ANALYSIS

THESIS

Alfred C. Anderson, LTC, USA
AFIT-ENP-MS-21-D-016

DEPARTMENT OF THE AIR FORCE
AIR UNIVERSITY

AIR FORCE INSTITUTE OF TECHNOLOGY

Wright-Patterson Air Force Base, Ohio

AFIT-ENP-MS-21-D-016

DEVELOPMENT OF A MAGNETIC CONFINEMENT ATTACHMENT FOR ENHANCED SIGNAL IN HANDHELD LASER INDUCED BREAKDOWN SPECTROSCOPY SOIL ANALYSIS

THESIS

Presented to the Faculty

Department of Engineering Physics

Graduate School of Engineering and Management

Air Force Institute of Technology

Air University

Air Education and Training Command

In Partial Fulfillment of the Requirements for the

Degree of Master of Science

Alfred C. Anderson Jr., MBA, BS

Lieutenant Colonel, USA

December 2021

AFIT-ENP-MS-21-D-016

DEVELOPMENT OF A MAGNETIC CONFINEMENT ATTACHMENT FOR ENHANCED SIGNAL IN HANDHELD LASER INDUCED BREAKDOWN SPECTROSCOPY SOIL ANALYSIS

THESIS

Alfred C. Anderson Jr., MBA, BS

Lieutenant Colonel, USA

Committee Membership:

LTC Michael B. Shattan
Chair

Dr. John D. Auxier II
Member

Dr. Gaiven Varshney
Member

AFIT-ENP-MS-21-D-016

Abstract

Field techniques for characterizing low levels of heavy elements of less than 100 parts per million in soils tend to be unreliable because of the relatively weak signal of these elements and the large, variable background inherent to analyzing soils with minimal sample preparation. To enhance the detection and analysis capability of a handheld laser-induced breakdown spectroscopy (LIBS) instrument, this work investigates the effects of a unique magnetic confinement apparatus on signal intensities, focusing on five iron lines as well as those from actinides in 11 soil samples. The proposed magnetic confinement apparatus achieved over 0.8 T but did not amplify the elements' peak intensities of the samples equally. Some peak intensities decreased with magnetic confinement. Through Principal Component Analysis (PCA), the difference in the intensity was attributed to elemental composition of the soil samples. Further conclusions were made based on the correlation of the samples' elemental composition and their spectral emission peak intensity increase due to magnetic confinement. The peak intensity increases were attributed to increased plasma density under magnetic confinement, which increased the rate of recombination as the plasma cooled. The magnetic confinement apparatus was designed for use with the SciApsZ300 handheld LIBS and is easily adaptable to other handheld models. This novel approach provides a simple, field-expedient means of improving handheld LIBS performance.

Acknowledgements

I am grateful to the committee members at AFIT and LANL for their assistance and help during this research. The insights and guidance provided kept the research on track and ensured a successful program.

I would like to thank my fellow students who supported each other every day and provided a measure of sanity in the frantic pace that was AFIT.

Special thank you to my wife who has kept me focused and reminded me that persistence and determination are not related to ability or intelligence. I depend on you more than you know.

Lieutenant Colonel Chuck Anderson, U.S. Army

Table of Contents

List of Figures

List of Tables

Development of a Magnetic Confinement Attachment for Enhanced Signal in Handheld Laser Induced Breakdown Spectroscopy Soil Analysis

Chapter 1: Introduction

1.1. Motivation

Following a nuclear incident, whether from an explosive device or a malfunctioning nuclear reactor, rapidly assessing the event's surrounding area is crucial for public safety, recovery, and providing a clear-picture for military and civilian decision-makers. Because most nuclear material does not fission before the device explodes, and instead becomes part of the fallout cloud along with dirt and debris, much fissionable material returns to the ground along with the rest of the fallout. The resulting concentrations of actinides in the soil are hazardous to humans, animals, and the environment. The species and concentrations of actinides present also provide valuable information for determining the type of device detonated. Therefore, after a nuclear event, the National Technical Nuclear Forensics (NTNF) Ground Collection Team (GCT) collects debris from the target environment for forensic analysis.

However, the analysis is not done on-site. The GCT sends the collected samples to a laboratory, which may not be on the same geographic land mass, and thus rapid acquisition of the elemental data is not possible. Although the laboratory analysis can eventually reveal the status and capability of suspected nuclear infrastructure and processes [1], immediate identification of actinides would be preferable for several reasons. On-site identification would help the GCT's ground commander to direct efficient and risk-minimizing debris-collecting activities. Faster analysis would also facilitate more effective resource allocation for emergency services and rescue operations. The NTNF, the Department of Defense

(DoD), and the Department of Energy (DoE) would all benefit from an immediate understanding of the actinides present in the sample material. Rapid elemental identification tools are not yet being used by the GCT.

In recent decades, laser-induced breakdown spectroscopy (LIBS) has advanced this objective, with the capability to provide information on actinides present in a soil sample in a matter of seconds. Handheld LIBS (HH-LIBS) allows rapid detection of areas with higher concentrations of actinides during the GCT's collection process. Knowing where actinides are present can reduce the total number and mass of samples required, reducing soldiers' exposure to a radioactive environment. Manard et al. showed that HH-LIBS enables rapid chemical analysis of rare elements, including uranium, to minimize exposure time and handling of hazardous nuclear materials [2]. HH-LIBS also offers the advantages of requiring only limited sample pretreatments and simplified sampling techniques [3]. However, HH-LIBS does not have sufficient sensitivity to detect concentrations of heavy metals such as actinides of less than 100-200 ppm [4]. Such concentrations are relevant to the safety, recovery, and decision-making concerns of on-site and departmental responders.

To improve the sensitivity of LIBS, this study attempts to demonstrate that magnetic confinement of the LIBS plasma in an HH-LIBS device amplifies spectral intensity and improves efficacy in a field environment. Section 1.2.2. LIBS Enhancement Methods describes other methods of improving LIBS sensitivity and their limitations.

1.2. Background

1.2.1. Current Radioactive Material Collection Methods

The GCT's procedure is to collect samples based on radiation dose, not on elemental composition. The GCT has access to several types of equipment for detecting α, β, and γ radiation, such as gamma scintillator probes, AN/PDR-77 radiation detection system, and personal dosimeters [1]. The GCT's mission is directed by the DoE. To limit exposure time while maximizing the amount of area covered and the number of samples collected, elemental analysis of radioactive material is not done at the collection site. Collected Samples are given to the DoE for analysis. To manage risk from nuclear exposure, members of the GCT wear electronic personal dosimeters on post-detonation collection missions [1], and this equipment shows both the current dose rate and the cumulative dose [5].

1.2.2. LIBS Enhancement Methods

Standard single-pulse LIBS analysis is hindered by low sensitivity and high limits of detection [6], which would make actinide identification difficult. However, there are a few ways to enhance the LIBS signal. Double-pulse excitation uses a second laser pulse to further excite the plasma elements after the first pulse's energy is absorbed by the plume [7]. However, the double-pulse technology is not yet supported in a handheld device. Another way to enhance the signal is through spark discharge (SD), where the laser is fired between electrodes that are only a few millimeters from each other and from the target. Using this technique, Nassef et al. (2005) found that as the voltage across the electrodes increased, the spectral line intensity increased by 150% to 400% [8]. A benefit of using SD-LIBS is the reduced surface damage to the sample because the spark affords a

significantly reduced laser pulse, and accordingly reduced ablation craters. The increase in intensity is quite impressive in a laboratory, however, this technology would be difficult to deploy by GCT members in a field environment. The GCT would need a mobile laboratory trailer, because the current geometry of HH-LIBS does not support SD-LIBS. A third way to enhance the emission intensity is Spatially Confined LIBS (SC-LIBS) which involves trapping the plasma plume inside a cavity, which typically has a hemispherical or cylindrical geometry [9]. To be beneficial, SC-LIBS would need to be designed inside of the HH-LIBS device because the plasma plume grows inside of HH-LIBS. A fourth way to enhance the emission intensity is through magnetic confinement which increases spectral line intensity by restricting electrons to a smaller space. This increases the number of collisions and thus improves the electron impact excitation [10]. Magnetic confinement affords the flexibility to be able to be adapted to commercial off-the-shelf HH-LIBS.

1.2.3. Portable and HH-LIBS

Portable LIBS was developed to meet the International Atomic Energy Agency's need for a portable technique with which inspectors of Los Alamos National Laboratory could quickly analyze the elements from hydrogen to plutonium [11,12]. This equipment was conceptualized as a multi-component system that could be packed and moved in a single box containing the laser and spectrometer [13]. The first suitcase LIBS was developed at Los Alamos National Laboratory for the United States DoE [13]. This device comprised a suitcase containing a charge-coupled device and controller board, power supplies, spectrograph, and photodiode, weighing 14.6 kg in total and measuring 46 x 33 x 24 cm, attached through fiber optics and power cables to a probe that contained the Nd:YAG laser [14]. In a further development, a backpack LIBS featured the spectrometer and

computer in a backpack tethered to a power supply and connected by fiber optics to a handheld probe [15].

Traditional LIBS components included a laser, at least one spectrometer, and a computer. For space travel, The Mars Science Laboratory (MSL) rover, Curiosity, required these components to be smaller and lighter because volume and mass were a premium when planning to leave the Earth. The Mars rover was used to perform remote rock and soil classification of light elements [16]. The MSL's Chemistry and Camera tool (ChemCam) was mounted and tested at Los Alamos National Laboratory [16], and was able to rapidly identify features of the Martian landscape from seven meters away using a telescope that was fiber-optically attached to three spectrographs [17]. The MSL's ingenuity facilitated the development of compact portable LIBS.

Several companies were able to take advantage of the technological advances. B&W Tek developed HH-LIBS for the pharmaceutical industry [18]. Hitachi Vulcan manufactures HH-LIBS to analyze alloys [19]. SciAps, Inc., was able to develop a commercially available HH-LIBS that is 30% smaller than the size and weight of the ChemCam [20]. However, for safety reasons, Commercial Off-The-Shelf (COTS) HH-LIBS does not have a telescope and cannot be used from seven meters away, requiring closer proximity to the target. In the space of an oversized hand drill, the SciAps Z500 contains a 5-mJ laser, a stack of spectrometers with a range from 180 to 680 nm that has a 0.1-nm FWHM optical resolution, and an argon purge [21].

1.2.4. Actinides in Soil

Actinides are the longest-lived of the radionuclides and the most harmful to people, plants, and wildlife for long term unprotected exposure [22]. Actinides remain even after

radionuclides with much shorter half-lives have decayed away. Actinides can be difficult to find in soil because of their low concentration and because actinides' slow decay rates can make them only slightly more radioactive than background radiation [23]. However, not all radiation is the same. Microwaves and radio waves are not ionizing. Alpha decay is an ionizing radiation that can cause cancer and death if exposed to or ingested internally. As actinides slowly decay through alpha decay, their daughter products rapidly produce ionizing radiation through beta decay. Actinides such as thorium and uranium decay through alpha decay, and therefore, they are hazardous to plants that grow in actinide-containing soils, and to humans or animals that have grazed on such plants [24]. Identifying actinides in soil through alpha spectrometry requires soil preparation to separate the actinides from the soil and from each other, and this process requires extensive laboratory time [25]. Moist soil can be particularly problematic because the laser's interaction with the water disturbs the spectrographic reading. Moisture can be removed by drying the soil at 105 °C, after which the soil is crushed and pelletized [26]. Although LIBS does not generally require sample preparation or treatment, Jantzi et al. have reported sample preparation methods, such as crushing, that increase LIBS sensitivity [27]. In addition, when analyzing soils with LIBS, the soil should be dried to remove moisture because otherwise the moisture absorbs some of the laser energy and can thus have an adverse effect on spectral intensity [28].

Thousands of tabulated uranium atomic emission lines have been reported in the literature [29–31]. However, the actinides are detectable only when the soil sample has a minimum actinide concentration of 0.26% by weight [29]. The low sensitivity of LIBS

hinders detection of trace elements [32,33]. In raw ore samples, the uranium detection limit is approximately 158 ppm [34]. A material weight of 0.26% is equal to 2600 ppm.

1.3. Problem

The challenge of this research is to develop a magnetic plasma confinement apparatus that will enhance the spectral lines of heavy elements in the soil. The apparatus needs to be compact enough to fit into a backpack and simple enough for use by GCT members. The apparatus also needs to be adjustable so it can be used with various models of HH-LIBS.

1.4. Hypothesis

This research is based on the hypothesis that it is possible to increase the spectral intensity of high Z trace elements by magnetically confining the plasma. Under magnetic confinement, the electron temperature and density of the plasma will increase [35]. The increase in density should increase the electron impact excitation, and thereby enhance the emission intensity [36]. For this research, permanent neodymium magnets secured around the nose cone of the HH-LIBS create the magnetic field.

1.5. Research Focus

This research focused on amplifying the spectral emissions of iron and uranium via magnetic confinement through the optimal configuration of permanent neodymium magnets using the soil samples provided by Los Alamos National Laboratory.

1.6. Methodology

Data was collected using the SciAps Z300 on various soil samples with and without magnetic containment. The experiment was repeated in the laser laboratory with a tabletop Nd:YAG laser for comparison. A frame around the HH-LIBS nose cone was developed to hold rectangular neodymium magnets for the magnetic confinement, and this device was used to ablate the soil samples. The gate delay was adjusted to find the best setting that maximized the integrated peak height of the magnetically contained plasmas.

Under magnetic confinement, the plasma's physical properties change during expansion across the magnetic field. The emission intensity increases because of the plasma's increased density due to its increased radiative recombination rate [37]. Magnetic confinement also slows plasma growth, thereby decreasing the volume of the plume.

1.7. Assumptions/Limitations

This study presumes the accuracy of the values presented in the National Institute of Standards and Technology (NIST) Atomic Spectra Database [38]. Assumptions were made based on the transition strengths and probabilities of spectral emissions from the database.

One of the limitations of LIBS was its low detection sensitivity of trace elements [33]. HH-LIBS alone may not have enough spectral expansion to positively identify the actinides present. Another limitation was the number of available soil samples with trace amounts of uranium or other actinides. Furthermore, the accuracy of the calibrations based on data collected from the Z300 HH-LIBS depended on the 0.1-nm resolution of the spectrometer [39].

Lastly, this study did not show whether combining magnetic and spatial confinement would further compress the plasma, increasing its density and thus the number of collisions, compared to the two confinements separately [40]. The greater the number of collisions, the more significant the number of excited atoms, and the greater the trace elements' spectral intensity. This regrettable limitation is due to the use of a commercial HH-LIBS that did not readily allow manipulation of the nose cone and plasma chamber.

1.8. Implications

This research advances the analytical capability of a commercial HH-LIBS device. This study confirms the spectral enhancement of heavy trace elements in soil via magnetic confinement and demonstrates the prototyping of a neodymium magnet attachment to HH-LIBS equipment. The magnetic confinement attachment enables trace element identification in metals, biological samples, and food testing.

Chapter 2: Theory and Literature Review

In 1957, Gordon Gould had the first recorded use of the acronym LASER, referring to Light Amplification by Stimulated Emission of Radiation [41].The acronym is now so ubiquitously known that “laser” has entered the common lexicon. Three years later, Theodore Maiman engineered the first functional ruby LASER [42]. Within a few years, spectrochemical analysis was being conducted on laser-induced plasma plumes, and LIBS became widely used as a rapid method of identifying materials based on their elemental composition [43]. The advantages of using LIBS for elemental analysis include its ability to find multiple elements simultaneously across the full range of the periodic table, with only optical access to the target [44]. This chapter begins with the theory of LIBS, followed by a discussion of the methods that are used to enhance the spectral intensity of the plasma emission.

2.1. LIBS Concept and Limitations

Laser-induced breakdown spectroscopy (LIBS) is a type of atomic emission spectroscopy where the excitation source is a highly energetic laser pulse [45]. A focused laser forms a plasma where the laser’s energy atomizes and excites the sample target [46]. The plasma, a partially ionized gas containing molecules, radicals, atoms, ions, and free electrons, has no overall electric charge. Atomization occurs at the beginning of the laser pulse, when the vaporized solid materials dissociate into atoms of the material’s constituent elements [47]. If the energy applied to the atom is greater than the ionization potential, electrons will detach from the atom, yielding free electrons and positive ions (cations). The

valence shell is the first to lose electrons because it has the lowest ionization potential [48]. An even greater laser energy can dissociate more electrons from the atom.

When the laser pulse ends, the atoms and ions return to lower energies or ground states as cations absorb free electrons. Electrons drop to lower energy shells, releasing their excess energy as light that creates spectral lines. The emissions occur as a continuum of energy. However, because of the different energies of the ions and the various energy transitions, cation deexcitation occurs through a discrete, quantized set of energy levels, which exhibit distinctive spectral lines for each element. It should be noted that even if no spectral lines for a given element are detected, that element may still be present in the sample, but at a concentration lower than the equipment's limit of detection [49].

All elements will emit light with distinctive frequencies when excited to high enough temperatures [50], and thus the focused laser must reach the energy level appropriate for the target material and its environment to create a plasma. With LIBS, plasma temperatures are typically 5,000 to 20,000 °C [45,51], and LIBS can analyze material in any physical state of matter—solid, liquid, or gas [52]. At the target surface, the detonation radiation indicates the elemental composition of the target through visible and ultraviolet wavelengths [53]. With a suitable laser power, and a spectrograph and detector with appropriate sensitivity and wavelength range, LIBS can detect all the elements on the periodic table. LIBS sensitivity can be as low as 10–50 ppm [53].

2.2. Methods of Signal Enhancement

Conventional HH-LIBS techniques can struggle to detect heavy elements in the soil because these elements are typically present at exceptionally low concentrations, and thus

present weaker spectral peaks [54]. LIBS spectra from soils are also notorious for their complexity and shot-to-shot variability because of soils' natural elemental heterogeneity and often-inconsistent moisture content. Therefore, several methods of enhancing the spectral intensity have been developed, including double-pulse LIBS, spark discharge (SD) LIBS, spatially confined LIBS, and magnetically confined LIBS.

2.2.1. Double-Pulse LIBS

Double-pulse LIBS (DP-LIBS) can increase emission lines by two orders of magnitude over that produced by single-pulse LIBS [55]. In DP-LIBS, two laser pulses, transmitted only nano- or micro-seconds apart, are used to produce the plasma [56]. The first laser pulse ablates the target, producing a plasma plume and a shockwave, and the second pulse is absorbed by the plasma [57]. The second pulse causes a resurgence in the plasma production following the initial pulse's plasma plume production, increasing the plasma volume further by ablating additional material in the gas phase. The second laser pulse also increases the plasma temperature and ion density [7,58]. Thus, the additional energy inputted to the plasma by the second laser pulse enhances the spectral line intensity from the first pulse, resulting in a significant signal gain [59]. The emission intensity increase may result from the additional heating of the target by the two pulses in combination, and the associated increase in plasma volume [60,61]. Figure 1 shows the different laser geometries that can be used in DP-LIBS: collinear, crossbeam, orthogonal re-heating, and orthogonal pre-ablation [62]. In the collinear arrangement, both laser beams are on the same axis perpendicular to the target. In the crossbeam arrangement, the lasers are both aimed at the same point on the target from different angles. In the orthogonal reheating arrangement, the first laser is perpendicular to the target, and the second laser is parallel to

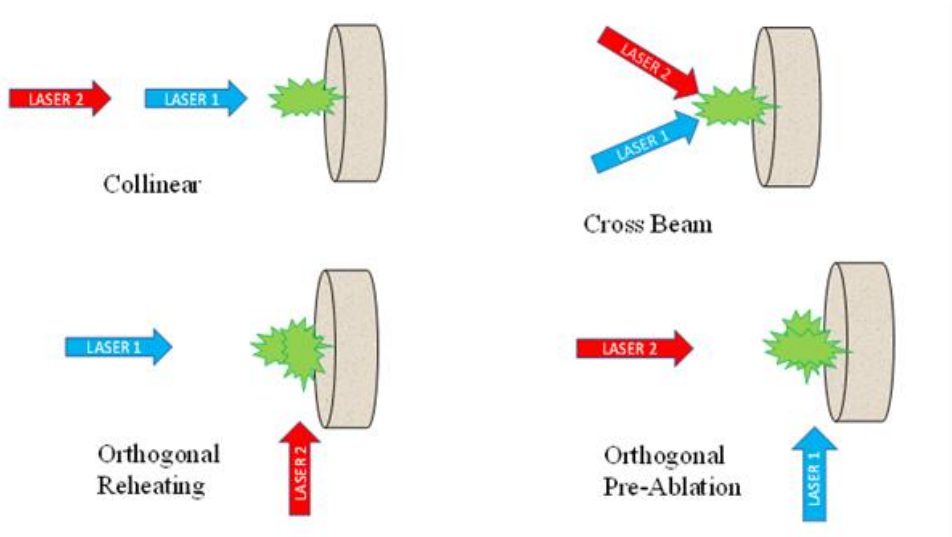

Figure 1. Four of the Double Pulse arrangements for LIBS.

the target and orthogonal to the first laser: the first laser creates the plasma, and the second laser is focused inside the plasma plume. In orthogonal pre-ablation, the reverse of orthogonal reheating, the first laser is parallel to the target and focused to create gas-phase plasma just above the target surface, and the second laser is perpendicular to the target and focused on the target surface for ablation [63]. Of the four different arrangements, collinear is the most common and crossbeam DP-LIBS is the least common [55].

2.2.2. Spark-Discharge LIBS

As with DP-LIBS, Spark-Discharge LIBS (SD-LIBS) is a two-part excitation process. Whereas DP-LIBS uses a second laser pulse to enhance the signal from the plasma plume, SD-LIBS enhances the signal by ablating the target between two electrodes, leveraging the voltage between the electrodes to expand the plasma plume [64]. SD-LIBS is triggered by the formation of the ablated target's plasma [8]. Compared to single-pulse LIBS, the spark discharge not only increases the plasma's spectral intensity but also offers a better signal to background ratio [65], and these advantages favor adding the electrical circuit to the

apparatus as an inexpensive approach to improving performance. Furthermore, SD-LIBS requires less laser pulse energy and therefore results in less damage to the target surface as shown in Fig. 2, where the left and right images show targets after analysis by conventional LIBS (five shots with laser fluence of 48 J/cm^2) and SD-LIBS (laser fluence of 4 J/cm^2 and applied voltage of 3.5 kV), respectively [8]. The crater depth after conventional LIBS is

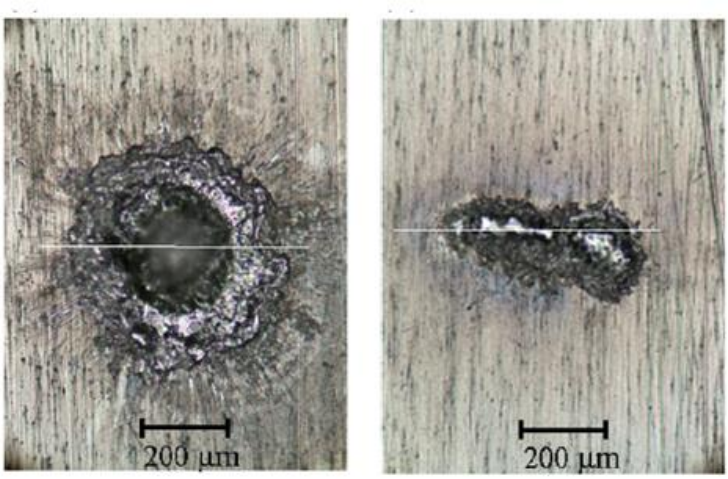

Figure 2. The laser fluence is much greater for conventional LIBS on the left causing more damage than what is required for SD-LIBS on the right to increase the spectral intensity [8].

more than 35 µm, whereas the SD-LIBS crater depth is only approximately 12 µm. Although the peak plasma temperatures are similar, the SD-LIBS plasma volume is larger. Finally, compared to DP-LIBS, SD-LIBS has a less complicated laser system and is thus also less expensive [66].

2.2.3. Spatially Confined LIBS

Another cost-effective method for increasing the detection sensitivity of plasma emission lines is spatial confinement [67]. Spatially-Confined LIBS (SC-LIBS) involves

trapping the plasma plume inside a cavity, which typically has a hemispherical or cylindrical geometry [9]. Confining the plasma stabilizes its shape and increases the electron density and temperature [68]. Spatial confinement can enhance the spectral emission within a specific range of delay time that depends on the cavity's size and the laser's energy [69]. Wang et al. (2016) showed that using a cylindrical cavity of 8 mm in both diameter and depth, the neutral copper line at 521.8 nm had as much as 2.5 times higher spectral intensity with delay times between 6 and 16 μs, compared to the intensity without the cavity [69].

Spatial confinement also reflects the plasma and accompanying shockwave back onto itself, increasing the number of collisions among particles and further amplifying the emissions [60]. The increased number of collisions likewise increase the number of atoms in high-energy states and improve emission intensity [70,71]. Therefore, the reflectivity of the cavity may increase the spectral enhancement [70]. Popov et al. (2009) used the back reflection of the shockwave inside a 4-mm spherical cavity to increase the spectral intensity of iron lines by 10 times [70]. Popov et al. (2010) also found that the reflected plasma enhanced the visible spectrum from 430 to 440 nm, but not the ultraviolet range [71]. Lin et al. (2013) showed that using SC-LIBS with a 20-mm conical cavity, the intensity of the neutral chromium line at 425.44 nm increased by 7% [72]. However, if layers of microparticles are allowed to accumulate on the cavity walls, they will degrade the cavity's reflecting properties, eroding the spatial confinement’s capacity to increase the spectral emission [70,71]. Nonetheless, spatial confinement is low-cost and is the simplest way of improving the spectral intensity discussed to this point.

2.2.4. Magnetic Confined LIBS

Although magnetic confinement has not been reported with a HH-LIBS system, the technique has been applied in other fields. In principle, the magnetic field confines the free electrons and increases the plasma density, accelerating the electrons and increasing their collision frequency, thereby increasing emission intensities and producing higher backgrounds due to inverse bremsstrahlung [73]. The magnetic field also increases the plasma's density by increasing the radiative recombination rate [37]. Leung et al. (1975) used magnetic confinement inside a small (30-cm diameter, 33-cm length) vacuum chamber with a tungsten wire to increase an argon plasma's density by a factor of 100 at 0.0008 torr and 60 volts [68]. The magnets were mounted on the exterior of the vacuum vessel, which had been specifically designed to allow relocation of the magnets to different positions [74].

Magnetic confinement increases spectral line intensity by restricting electrons to a smaller space, which increases the number of collisions and thus improves the electron impact excitation [10]. Magnetic confinement also slows down the plasma growth [75], which will decrease the volume of the plume, such that it remains at the focal point of the light collection optics. Several conditions affect the relative impact of the magnetic field on emission intensity. First, the closer the magnetic field is to the plasma plume, the greater the effect magnetic confinement will have on the emission intensity [33]. In addition, specific wavelengths may be particularly influenced by the magnetic field's effects on emission intensity from electron impact excitation and radiative recombination [36]. The presence of an external magnetic field can also change a plasma's physical properties, which will affect the optical emission spectrum [37].

The relationship between a plasma's initial kinetic energy and magnetic confinement can describe the plasma's expansion and emission inside the magnetic field. Huba et al. estimated the endpoint of the plasma expansion via its kinetic energy as a function of magnetic field strength as in Eq. (1): where the expansion volume, $(4/3)\pi R_B^3$, is a function of the magnetic confinement radius R_B; M is the plasma's mass; v_0 is the initial plasma expansion velocity; and B_0 is the magnetic field (in G) [76].

$$\frac{1}{2}Mv_0^2 = \left(\frac{B_0^2}{8\pi}\right)\left(\frac{4}{3}\pi R_B^3\right) \quad (1)$$

Solving for the magnetic confinement radius of the plasma, R_B, yields

$$R_B = \left(\frac{3Mv_0^2}{B_0^2}\right)^{1/3} \quad (2)$$

Assuming a perfectly conducting plasma, the magnetic field will cause the outward expansion of the plasma to slow close to the magnetic confinement radius [76]. This deceleration of the plasma expansion is given as

$$\frac{v_2}{v_1} = \left(1 - \frac{1}{\beta}\right)^{1/2} \quad (3)$$

Where v_1 and v_2 are the plasma expansion velocities without and with magnetic confinement respectively [37,77,78]. Alfven's magnetohydrodynamics equation [79,80], shows that the magnetic field has an inverse relationship with plasma β, given by

$$\beta = \frac{8\pi n_e kT_e}{B^2} \quad (4)$$

Where n_e is the plasma's electron density in cm^{-3}, k is the Boltzmann constant, and T_e is the electron's temperature in eV [32,45,76,77,81]. As the magnetic field, B, approaches zero, plasma β approaches infinity, and the velocity ratio will approach one. The ratio of

emission intensity with magnetic confinement to the intensity without magnetic confinement can be expressed as

$$\frac{I_2}{I_1} = \left(1 - \frac{1}{\beta}\right)^{-3/2} \left(\frac{t_1}{t_2}\right)^3 \quad (5)$$

Where I_2 and I_1 are the intensities with and without magnetic confinement and t_1 divided by t_2 is the spectral emission ratio [32,81]. As with Eq. (3), when the magnetic field approaches zero, plasma β approaches infinity, and the intensity ratio will move towards one.

Rai et al. enhanced the optical emission intensities of magnesium, titanium, chromium, and manganese in aqueous solutions by 1.5–2 times using 0.5 or 0.6 T magnetic fields generated by neodymium magnets [37,81]. Harilal et al. reported that in a vacuum, a 0.64 T magnetic field decelerated the growth of a laser-generated aluminum plasma in the direction normal to the target surface, with the plasma instead growing laterally and expanding along the magnetic field lines [75]. The magnetic field also increased the plasma plume's lifetime, temperature, and density [75]. The magnetic confinement increased the spectral emission of Al^{2+} and decreased that of Al^{+} and neutral Al [75]. However, Shen et al. showed an increase in the neutral lines of aluminum with a magnetic containment field of 0.8 T [77]. The difference can be attributed to the vacuum environment in which Harilal et al. worked and the lesser magnetic field strength of 0.64 T. In LIBS analyses of steel samples, Hao et al. used a ring magnet to spatially and magnetically confine a plasma plume, and successfully increased the spectral intensities of vanadium and manganese [32]. Hao et al. also found that magnetic confinement increased the plasma's temperature and density [32]. However, Cheng et al. reported that magnetic confinement decreased the

plasma temperature compared to unconfined plasma when they studied the effects of a 0.75-T magnetic field on the spectral intensity of ablated copper [33].

Chapter 3: Methodology

3.1. Original Z-300 HH-LIBS Specifications and Operating Conditions

The SciAps Z-300 HH-LIBS, shown in Fig. 3, is a 5–6-mJ/pulse, 50-Hz, 1064-nm Nd:YAG laser with multiple spectrometers that cover the spectral range from 190 to 950 nm. The Z-300 measures 8.25 × 11.5 × 4.5 inches (21 x 29.2 x 11.4 cm) and weighs four pounds (1.81 kg), including the rechargeable Li-ion battery, and can transfer data via USB

Figure 3. The SciAps Z300 HH-LIBS used in this study.

and Wi-Fi [39].

Although the Z-300 can detect at least one spectral line for every naturally occurring element on the periodic table [39], the manufacturer does not formally claim that the equipment can detect transuranic elements because these elements are not typically found in nature [82]. Nonetheless, the Z-300 may still detect transuranic material. The equipment has been reported to detect uranium in an ore sample, although not always reliably [83].

In the Z-300, the laser is perpendicular to the faceplate, and the camera inside the nose cone is off-axis, resulting in some parallax in the view. For safety, the laser will not fire without a sample present in front of the camera. Therefore, optimal operating conditions include the positioning of the sample flush with the faceplate. Furthermore, if the sample is smooth and flat and in direct contact with the faceplate, completely covering the window, then the plasma plume's geometry will be entirely contained within the chamber behind the faceplate. By contrast, if the target sample is curved, rough, or not flush with the window, the plasma may occur slightly in front of the faceplate.

When the laser fires, argon is injected into the plasma chamber to purge the ambient air. The argon purge helps prevent the plasma plume from interacting with ambient air. The plasma chamber is an inverted trapezoidal pyramid with a base of only 20×15 mm^2 and a depth of 5 mm. Because the plasma plume must be captured within the chamber, enhancement through spark discharge is not possible with this equipment.

The disadvantage of the Z-300 is that improving the plasma chamber's geometry may not be possible because of the device's compact size and the laser's fixed focus on the outside edge of the faceplate. Ideally, as in a laboratory situation, the laser's focal point and the plasma chamber's geometry can be changed, and the trapezoidal pyramid geometry of the Z-300's plasma chamber may be unfavorable relative to the hemispherical or cylindrical geometries used in spatial confinement. Thus, the magnetic confinement approach to magnifying the spectral intensity proposed for this HH-LIBS could be further improved by spatial confinement if the plasma chamber's geometry could be manipulated. For example, a hemispherical container would reflect the plasma to the center uniformly, thereby increasing the emission intensity [71]. A cylindrical box would also reflect the

plasma onto itself and increase the number of particle collisions, increasing the number of atoms at high energy states and thereby enhancing the emission intensity

3.2. Z-300 Modification with Magnets

To conserve the Z-300's functionality, research began with small ring magnets of neodymium, as the least intrusive modification that would accomplish the objective of introducing a magnetic field that can influence the nose cone's plasma emission. Thus, magnetic confinement did not require changes to the HH-LIBS device, representing one of the most significant advantages of the magnetic confinement approach, that it can easily be adapted to commercial HH-LIBS devices.

To determine which polarity provides greater spectral intensity, data was collected from a soil sample with a ring magnet under the sample in both polarity configurations, flipping the magnet between data acquisition runs. Data was also taken with magnets held manually on the sides of the nose cone; however, this procedure indicated the need for a mechanism to secure the magnets in place such that they could not snap together.

3.3. Magnetic Apparatus Design

To optimize the configuration of permanent neodymium magnets, several tests using the using soil samples provided by Los Alamos National Laboratory were conducted with varying degrees of success. Magnetic field strength was measured between 0.3 and 0.8 T.

3.3.1. Ring Magnet

In a field environment, soil samples must be manually converted into pellets on-site using a stainless-steel die set. This presents a challenge for magnetic confinement with a

ring magnet because the pellet must be pressed inside the magnet and the stainless-steel die sets are strongly attracted to the permanent ring magnet, such that a table vice would be needed to separate the pieces.

Another issue with the stainless-steel die is that with the pellet inside the die sleeve, the pellet must be flushed with the sleeve's surface to contact the Z-300's faceplate. If the pellet is not flushed, the Z-300 may not detect the target and will not fire, or, if the Z-300 does fire, the plasma plume will not form in the optimal position for the spectrometer, resulting in weak readings. For this work, the pellet conditions were satisfied by using the ring magnet as the die sleeve and using a ceramic pressing rod and top support plate instead of the usual stainless-steel. Only one pressing rod was used so that the pellet would be flushed with the magnet's edge.

The original stainless-steel sleeve and dyes are shown in Fig. 4A. These did not allow for the pellet sample to be flushed with the Z-300's faceplate. To ensure a flush sample position, a smooth dye was produced, along with a dye with a raised cylinder that would slide into the ring magnet, as shown in Fig. 4B. The new dyes were made of carbide steel, which is not so strongly attracted to the magnet as stainless steel.

Nonetheless, because the carbide is magnetic, pulling the dye away from the ring magnet would loosen the pellet's grain structure, negating the benefit of pressing it. Furthermore, because of the tight tolerance between the inside of the ring magnet and the

raised cylinder of the carbide dye, tiny magnetic particles between the magnet and the dye disturb the fit so that the dye no longer sits well in the magnet.

A **B**

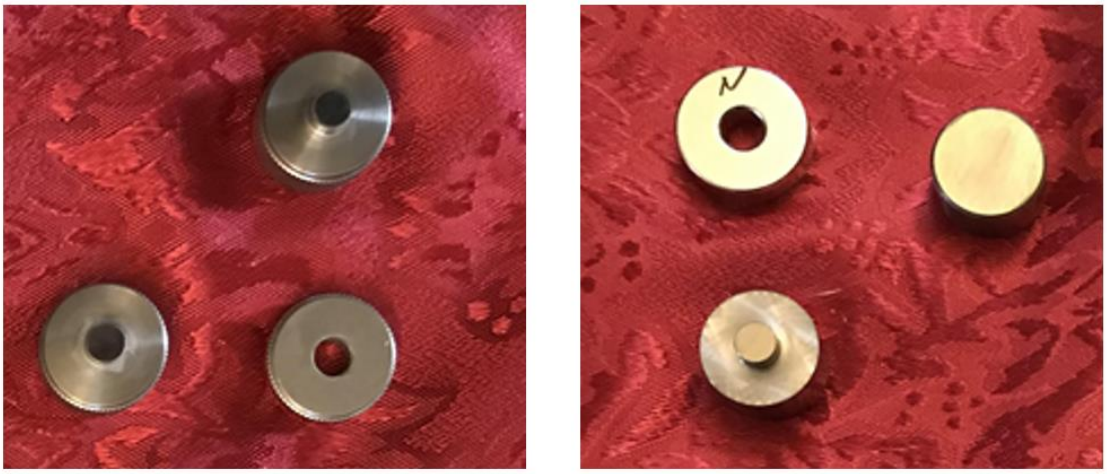

Figure 4. (A) Original stainless-steel dyes and sleave. (B) Ring magnet used as sleave with carbide dyes

3.3.2. Three Magnets

The next attempt to create a magnetic apparatus involved attaching one magnet on either side of the Z-300 with a third magnet under the soil sample, as show in Fig. 5A. Although this configuration showed a magnetic field of approximately 0.25 T, as illustrated in Fig. 5B, the sample was crushed in the process. The magnetic field shown in Fig. 5B was calculated using finite element method magnetics [84].

A B

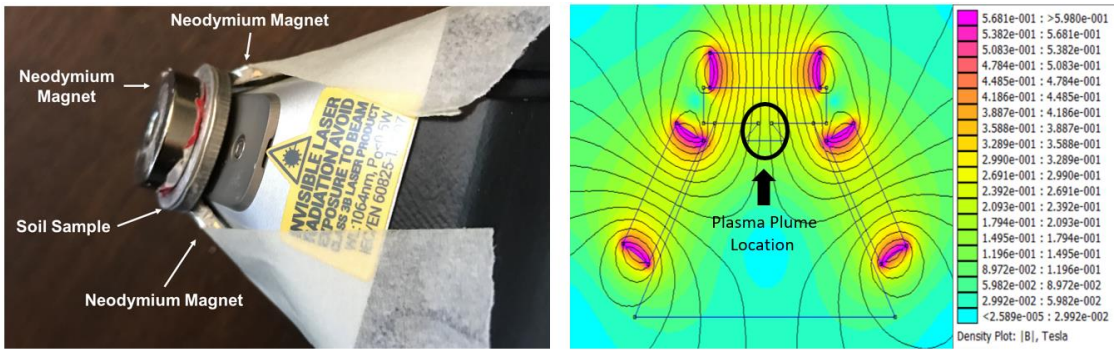

Figure 5. (A) Neodymium magnets around Z-300 and soil sample. (B) FEMM calculated magnet field of the magnets around nose cone [84].

3.3.3. Magnetic Confinement Frames

To avoid destroying the soil samples in the magnetic confinement approach, a simple wooden frame was designed to hold the magnets, as shown in Fig. 6A. The frame was also adjustable so that the magnets could be fitted snugly to the nose cone. The magnets were

A B

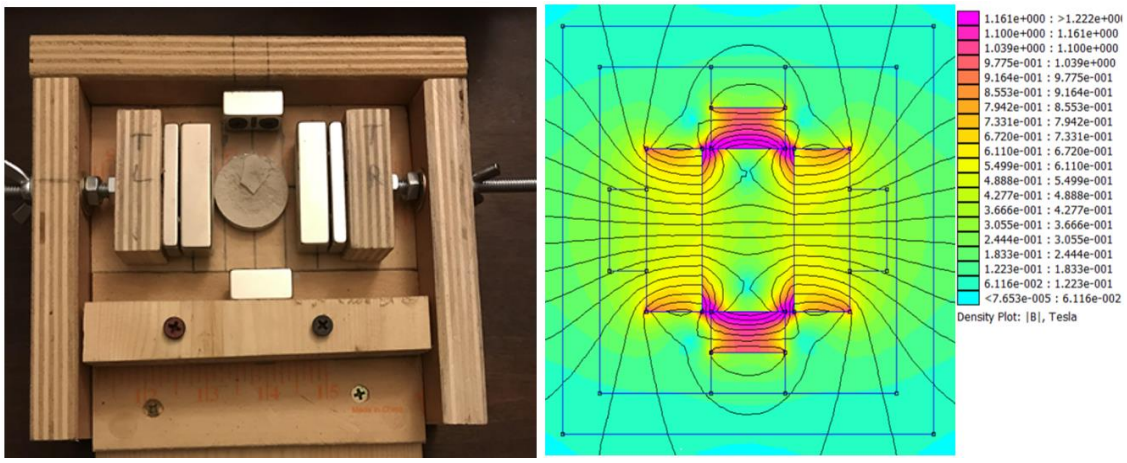

Figure 6. (A) Neodymium magnets and soil sample in wooden frame. (B) FEMM calculated magnet field of the wooded frame [84].

arranged so that all the north sides face right, and all the south sides face left. Figure 6B shows the calculated magnetic field, which was 0.3 T at the center. Experiments showed that the bottom magnet interfered with determining if the Z-300 was properly seated between the magnets and flush with the soil sample. The bottom magnet also had the least plasma enhancement effect because it was the furthest away, at 5 cm from the plasma.

The wooden prototype provided a proof of concept, but it lacked the ability to change the magnets since they were screwed into the frame. The AFIT Model Shop provided the functionality required to change the magnets with an aluminum frame apparatus. The aluminum frame is designed to hold up to four magnets. The magnets are mechanically held in place with clamps that allow a 13 mm magnet to be secured as shown in Fig. 9A. The magnetic field generated with this arrangement is shown in Fig. 9B. With this frame,

A **B**

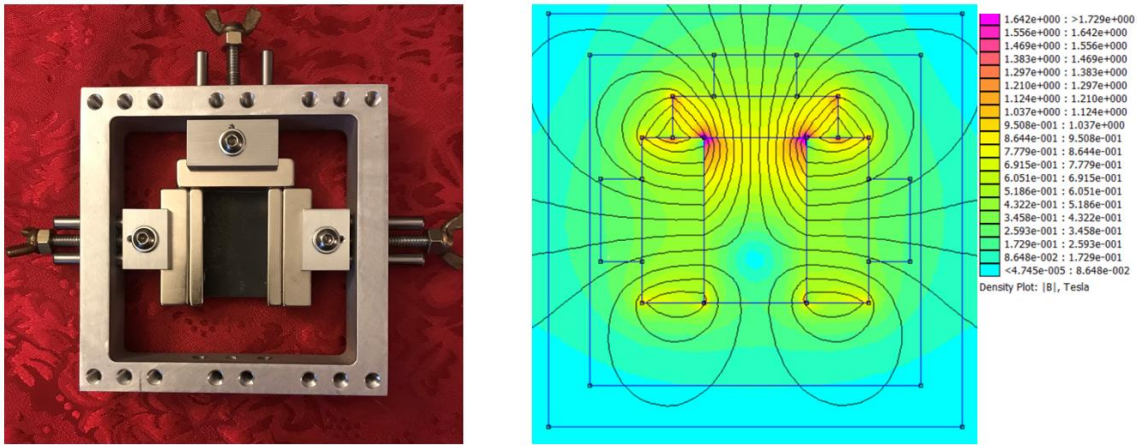

Figure 7. (A) Neodymium magnets and soil sample in aluminum frame. (B) FEMM calculated magnet field of the aluminum frame [84].

the magnets had a different arrangement from that in the wooden frame. The top magnet's field orientation is like the magnets on the right and left. The north side of the top magnet

faces the center of the frame, while the north sides of the left and right magnets face the frame's edge. The frame's interior dimensions measure 10.3 × 10.3 cm and can hold up to four permanent magnets that are 3.3 cm in width, on all four sides of the frame. The positions of the magnets can be adjusted towards and away from the center. This aluminum frame became the final design for the magnetic containment apparatus, fitted around the nose cone of the Z-300 HH-LIBS device. The apparatus can also be mounted on a table for use with a tabletop laser. The magnets on the sides of both frames were limited to a minimum separation of 33 mm due to the size of the soil sample. If the soil samples had been less than 22 mm, the sample would not have passed the edges of the face plate of the Z-300, which would have allowed for closer magnets and a higher magnetic field.

3.4. Soil Samples

The main advantages of using LIBS on soil samples are the technique's rapid analysis capability and minimum sample preparation [85]. The soil samples for all experiments, with and without magnetic confinement, were provided already grounded and pressed by Los Alamos National Laboratory, along with a spreadsheet listing their trace elements in parts per million. Fig. 8 shows a typical soil sample. Samples were sorted by their amount

Figure 8. Soil Sample GBW07311 from Los Alamos National Laboratory.

of data on trace elements. Samples were discarded if their trace element data was incomplete. The remaining samples were ordered by their quantity of actinides. Only two

Table 1. The Actinides in the LANL soil samples.

Sample Name	Rock Type	Composition Type	Thorium (ppm)	Uranium (ppm)
GBW07103	Igneous	High SiO2	54	18.8
GBW07311	Sedimentary	Phyllosilicate	23.3	9.1
GBW07312	Sedimentary	Phyllosilicate	21.4	7.8
GBW07113	Igneous	High SiO2	27.1	4.83
GBW07110	Igneous	Medium SiO2	16.7	3.04
JA2	Igneous	Medium SiO2	5	2.2
AGV2	Igneous	Medium SiO2	6.1	1.86
BCR2	Igneous	Low SiO2	5.7	1.69
GBW07104	Igneous	Medium SiO2	2.6	0.9
BHVO2	Igneous	Low SiO2	1.22	0.403
JA1	Igneous	Medium SiO2	0.76	0.35

actinides were listed in the soil samples, thorium and uranium, as shown in Table 1. Because uranium decays into thorium, the correlation between these two elements in the soil is high. The samples had a Pearson coefficient of r = 0.9565 of uranium and thorium. This is not to say that none of the thorium is naturally occurring.

Selecting suitable emission spectral lines for analysis can be difficult because there are 474 uranium and 20,143 thorium spectral lines in the National Institute of Standards and Technology (NIST) database [38]. Chinni et al. (2009) reported that double-pulse LIBS increased six uranium spectral lines: 367.01, 409.01, 436.20, 437.21, 447.23, and 591.54, where the uranium concentration in their sample was 0.26% [29]. This concentration is much greater than that in the soil samples used in this study. Kim et al. reported that the minimum observable concentration of uranium in ore was approximately 158 ppm [34]. Using HH-LIBS to find uranyl fluoride surface contamination, Shattan et al. chose the

uranium spectral lines U II 409.013, U I 502.739, U I 509.539, U I 682.691 nm for their high intensity and their observability even at lower uranium concentrations [86]. Of these, U II 409.013 nm was observable at the smallest concentration of 250 ppm [86]. Because the soil samples used for this work had uranium concentrations well below the previously mentioned limits of detection, the emission lines selected for analysis were those that were most prominent in previous studies as shown in Table 2.

Regarding the other actinide in the soil samples, approximately three times more thorium was present than uranium, in ppm, which is their estimated relative abundance in nature as well [87]. Thorium can be characterized by 12 spectral lines with relative intensities greater than 30,000 [38]. The highest thorium spectral line was beyond the spectrometer; therefore, 11 wavelengths were selected for analysis under magnetic confinement in this work.

Table 2. Prominent uranium lines from previous studies.

U neutral and ion	Atomic Line (nm)	Reference
Uranium I	356.66	[29,34,38,67]
Uranium I	358.49	[34,38,92]
Uranium I	367.01	[29,38]
Uranium II	409.01	[13,29,34,38,67,86]
Uranium I	436.2	[29,38]
Uranium II	447.23	[29,38]
Uranium I	502.74	[13,29,38,86]
Uranium I	591.54	[13,29,38]
Uranium I	682.69	[13,29,38,86]

Although plutonium is another important detection target after a nuclear event, the soil samples used for this research contained no plutonium. The soil samples do contain

between 3.0-19.3% iron, which is higher than the average of 4% by weight across all soils [88]. The five iron lines that were chosen for analysis are Fe II 259.940, Fe II 273.955, Fe II 274.320, Fe II 274.698, and Fe II 275.574 nm. Iron lines are prolific throughout the spectrum. Their spectral lines often overlap other elements' spectral lines. The five iron lines were chosen because their location on the spectrum is not overly populated with plutonium spectral lines [89]. In an actinide-rich environment, these iron lines can be used to facilitate a baseline.

3.5. Comparison with EverBright LASER

Following testing with the Z-300 HH-LIBS, the magnet confinement apparatus described above was also used in conjunction with a tabletop Quantel EverBright 1064-nm laser and a Catalina Scientific Echelle spectrometer as shown in Fig. 9. The five iron lines analyzed with the HH-LIBS are more than 50 nm less than the spectrometer's ability to read because the Catalina Scientific spectrometer detects wavelengths only at or above 325 nm. Samples GBWO7113 and GBWO7311 were chosen and tested with/without magnetic

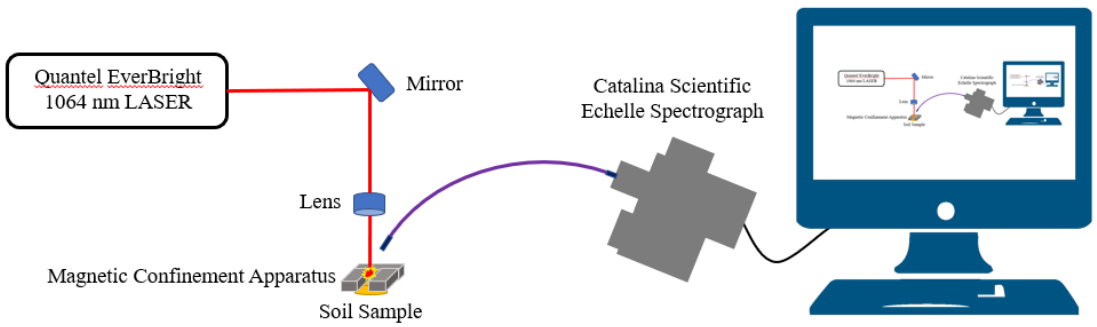

Figure 9. The Experimental setup with the Quantel Everbright LASER and Catalina Scientific Echelle Spectrograph used in ambient air with/without magnetic confinement apparatus.

confinement because of their relatively high thorium and uranium concentrations as shown in Table 1. Both the EverBright and the Z-300 use a 1064 nm laser. Unlike a 532 nm laser, it cannot be seen because the wavelength is in the infrared and outside of the visual spectrum. At 150-250 mJ /pulse the EverBright Laser is about 40x more powerful than the 5-6 mJ /pulse Z-300 [39,90]. Using the EverBright laser, the gate width was tested between 2 and 10 μs, and the gate delay was also varied between 2 and 10 μs. After several shots, the optimal settings were a gate width of 10 microseconds and a gate delay of two microseconds. Chinni et al. [29], Liu et al. [91], Yin et al. [68], Sobral et al. [92], Rai et al. [37], and Chan et al. [93] used gate widths of 10 microseconds or larger. Samples were shot five times each with and without magnetic confinement. The soil sample when tested is placed beneath the magnetic confinement apparatus. The apparatus was adjusted to increase the magnetic field by bringing the sides close together, while still leaving space so that the fiber optic cable could view the plasma as shown in Fig 10. The fiber optic cable was positioned approximately 85mm from the plasma plume. The data was averaged and

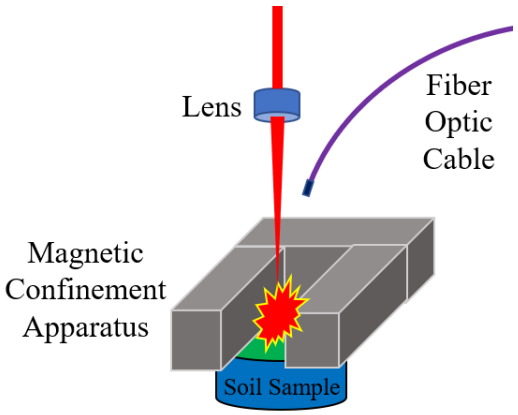

Figure 10. Magnetic confinement apparatus in relation to soil sample while being tested using the Quantel Everbright laser.

plotted with MATLAB. Another difference between the EverBright and the HH-LIBS experiments was that the HH-LIBS has an argon flush to limit the plasma's interaction with ambient air. In contrast, the EverBright experiment was performed in ambient air without the benefit of a noble gas flush. The locations of the magnets in the aluminum frame shown in Fig. 11A were adjusted to increase the magnetic field by positioning the magnets much closer together, as they no longer had to be situated around a nose cone. One of the advantages of the magnetic confinement apparatus is that it is adjustable to fit the lab scenario. The gap between the magnets was 13 mm, which allowed a sufficient angle for the spectrometer to view the plasma plume and for the laser to clear the magnets without ablating them. The corresponding magnetic field increased by approximately 0.1 T to over 0.8 T, as represented in Fig. 11B.

A **B**

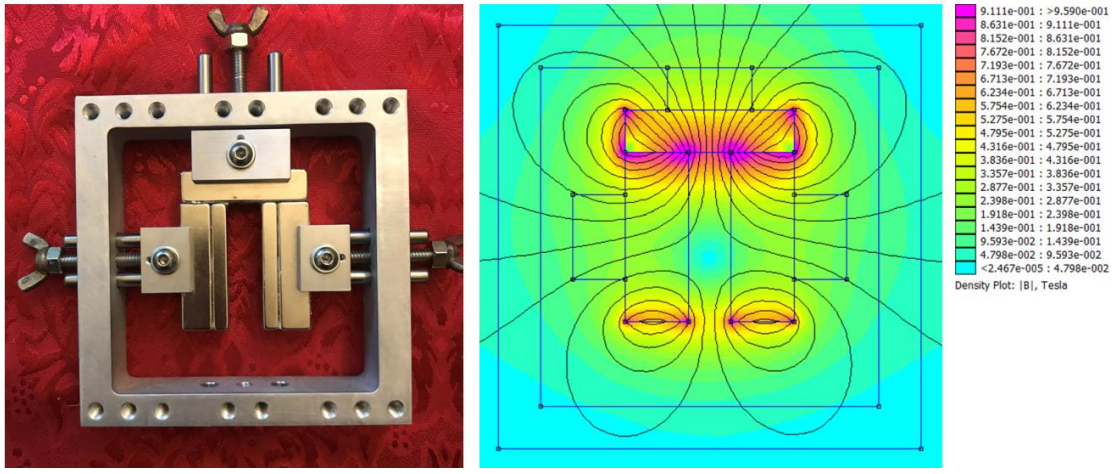

Figure 11. (A) Neodymium magnets configured in aluminum frame. (B) FEMM calculated magnet field of the aluminum frame [84].

3.6. Testing and Analyzing Procedures

Los Alamos National Laboratory provided certified reference material in the form of 23 soil samples. The final test with the aluminum frame had magnets on three sides of the Z-300. The Z-300 was also inverted to allow a more consistent magnet placement and target position as shown in Fig. 12. Of the available soil samples, 11 were chosen for this

Figure 12. Test set up of the Z-300 inverted with neodymium magnets configured in aluminum frame and soil sample.

test. The criteria for the chosen 11 samples was they had to have the most complete elemental composition data as shown in Table 3 and Table 4, and they had to still be in good testing condition after previous tests while prototyping the optimal magnetic confinement apparatus. Some samples were not considered in good condition because of damage due to shipping, pitting due to LIBS testing, or they were crushed due to magnetic confinement. Each of the 11 samples was tested with and without magnetic confinement for a total of 16 times each. The data from the unconfined test and from the magnetically

confined test were pulled into MATLAB and averaged into groups by sample name and plotted.

Table 3. Lanthanides and Actinides in the 11 soil samples.

Soil Sample	Ce ppm	Dy ppm	Er ppm	Eu ppm	Gd ppm	Ho ppm	La ppm	Lu ppm	Nd ppm	Pr ppm	Sm ppm	Tb ppm	Tm ppm	Yb ppm	Th ppm	U ppm
GBW07104	40	1.85	0.85	1.02	2.7	0.34	22	0.12	19	4.9	3.4	0.41	0.15	0.89	2.6	0.9
JA2	33.7	2.9	1.7	0.91	3	0.61	16.1	0.25	14.2	3.7	3.1	0.48	0.26	1.68	5	2.2
JA1	13.5	4.8	3	1.12	4.2	1.05	5	0.45	10.9	2.08	3.4	0.73	0.44	3	0.76	0.35
GBW07312	61	4.8	3.1	0.61	4.4	0.04	32.7	0.58	26	6.9	5	0.82	0.53	3.7	21.4	7.8
AGV2	68.6	3.47	1.81	1.53	4.52	0.65	37.9	0.247	30.5	7.84	5.49	0.64	0.26	1.62	6.1	1.86
GBW07110	117	5.32	2.93	1.96	6.54	1.1	62.5	0.49	47.2	13.2	8.63	0.99	0.5	3.15	16.7	3.04
BCR2	52.9	6.41	3.66	1.96	6.75	1.28	24.9	0.503	28.7	6.7	6.58	1.07	0.54	3.38	5.7	1.69
BHVO2	37.5	5.31	2.54	2.07	6.24	0.98	15.2	0.274	24.5	5.35	6.07	0.92	0.33	2	1.22	0.403
GBW07311	58	7.2	4.6	0.6	5.9	1.4	30	0.78	27	7.4	6.2	1.13	0.74	5.1	23.3	9.1
GBW07113	163	8.19	4.31	1.18	9.47	1.64	82.7	0.67	64.5	18.4	11.7	1.51	0.73	4.51	27.1	4.83
GBW07103	108	10.2	6.5	0.85	9.3	2.05	54	1.15	47	12.7	9.7	1.65	1.06	7.4	54	18.8
Group	Lanthanides														Actinides	

Table 4. Additional trace elements of the 11 soil samples.

Soil Sample	Rb ppm	Cs ppm	Sr ppm	Sc ppm	Y ppm	Zr ppm	Hf ppm	V ppm	Nb ppm	Ta ppm	Cr ppm	Co ppm	Cu ppm	Zn ppm	Pb ppm	Cl ppm	F ppm
GBW07104	38	2.3	790	28	29	99	2.9	94	6.8	0.4	32	43.2	55	71	11.3	46	280
JA2	71	4.9	250	18.4	18.1	112	2.93	122	9	0.7	450	27	27.9	65	19.3	0	223
JA1	10.65	0.64	264	9.5	9.3	84	2.5	108	1.4	0.11	6.4	11	41	91	5.8	43	149
GBW07312	270	7.9	24	32	26	234	8.3	47	15.4	3.2	35	8.8	1230	498	285	163	1250
AGV2	66.3	1.2	661	33	37	230	5	122	14.5	0.87	16	16	53	86	13.2	0	377
GBW07110	183	7.16	318	5.1	29	335	7.5	64.3	20.8	1.42	7.7	7.9	9.1	164	97.7	160	1120
BCR2	46.9	1.1	340	7.4	42.7	184	4.9	416	12.6	0.74	18	37	21	127	11	98	448
BHVO2	9.11	0.1	396	13	19	172	4.36	317	18.1	1.14	280	45	127	103	1.6	150	402
GBW07311	408	17.4	29	7.52	28	153	5.4	46.8	25	5.7	40	8.5	78.6	373	636	290	1650
GBW07113	213	3.34	43	5.15	42.5	403	10.8	3.8	34.3	2.41	7.3	2.4	10.9	86.3	33.3	0	1300
GBW07103	466	38.4	106	6.1	62	28	6.3	24	40	7.2	3.6	3.4	3.2	167	33.3	127	2350
Group	IA	IA	IIA	IIIB	IIIB	IVB	IVB	VB	VB	VB	VIB	VIIIB	IB	IIB	IVA	VIIA	VIIA

Table 5 shows the large elemental composition in soil samples. Elements are in order of abundance in parts per million. Soil Samples are in order of increasing benefit of magnetic confinement.

Table 5. Large elemental composition in soil samples.

Soil Sample	O ppm	Si ppm	Fe ppm	Al ppm	Ca ppm	K ppm	Na ppm	Mg ppm	Ti ppm	C ppm	Mn ppm	P ppm	H ppm
GBW07104	538,655	283,351	68,541	85,578	37,164	15,690	22,760	10,372	3,090	9,470	604	1,030	945
JA2	562,555	263,719	87,577	81,556	44,954	14,943	18,338	45,830	3,956	-	836	64	705
JA1	564,412	299,009	98,100	80,550	40,737	6,334	22,642	9,468	5,094	-	1,216	720	453
GBW07312	541,039	361,270	86,761	49,219	8,290	24,157	2,594	2,834	1,510	4,491	1,400	235	1,354
AGV2	566,068	277,181	93,580	89,495	37,164	23,908	24,706	10,794	6,293	-	770	2,095	-
GBW07110	540,735	294,756	66,040	85,208	17,653	42,918	18,043	5,065	4,795	2,811	689	1,571	1,127
BCR2	640,177	252,875	193,035	71,448	50,885	14,860	18,633	21,649	13,545	-	1,549	1,527	-
BHVO2	483,347	233,243	172,053	71,448	81,474	4,317	13,090	43,599	16,362	-	1,290	1,178	126
GBW07311	524,357	356,440	66,848	54,882	3,359	27,146	2,712	3,739	2,100	2,646	2,490	255	1,681
GBW07113	524,333	340,189	44,861	68,590	4,217	45,077	15,154	965	1,798	1,419	1,084	196	743
GBW07103	518,334	340,423	29,934	70,918	11,078	41,590	18,456	2,533	1,720	409	463	405	378

3.7. Principal Component Analysis

Principal Component Analysis (PCA) is a data analysis technique that reduces data from high dimensional space to low dimensional space while still maintaining the underlying variance of the data [94]. Complex data sets that are composed of multiple variables are reduced by PCA to a set of eigenvectors with eigenvalues that contain the data set's variation. The largest eigenvalue shows the eigenvector that contains the largest amount of variation [94]. PCA's goal is to calculate the most important basis by filtering out noise to display meaningful data [45].

The goal of principal component analysis is to compute the most meaningful basis to re-express a noisy data set. PCA creates a new basis that removes the noise to reveal a hidden structure [95]. For this research PCA provides a quantitative method to determine a correlation within the samples' elemental composition and their spectral intensity with and without magnetic confinement. The first principal component shows the most variance between the samples tested, while the second principal component shows the second most variance between the samples tested. The number of principal components is limited by the number of features in the samples.

3.8. Integrated Area Calculation

To compare the size of the spectral intensity of the selected emission lines, the integrated area below the curve (I_B) is subtracted from the integrated area under the curve ($I_A + I_B$) to get the integrated area of just the curve (I_A) as shown in Fig. 13. For each

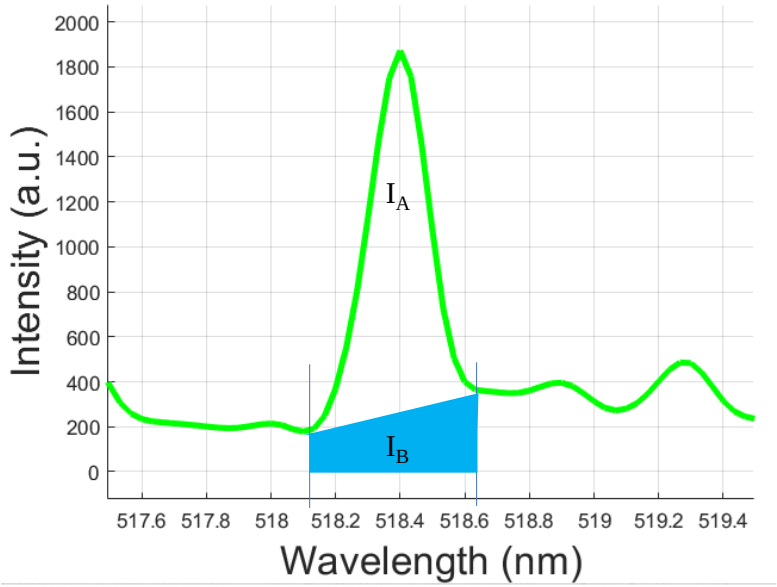

Figure 13. The integrated area under the curve (I_B) is subtracted from the integrated area of the curve ($I_A + I_B$).

sample's spectral lines of interest, the I_A with magnetic confinement is compared to the I_A without magnetic confinement. For trace elements to see if emission intensity is statistically significant, I_A must be greater than three times the square root of I_B [96].

Chapter 4: Results

This chapter will discuss the results of the performance tests described in the previous chapter to evaluate the capacity of the proposed magnetic confinement apparatus for improving signal and detection performance of the Z-300 HH-LIBS. The emission intensities of the uranium, thorium, and iron lines are reported, with and without magnetic confinement, for all 11 soil samples. A principal component analysis provides insight into the variation of spectral enhancement due to magnetic confinement. This chapter will conclude with the correlation of trace elements in the Los Alamos National Laboratory certified soil samples with the benefit or detriment due to magnetic confinement.

4.1. Iron (Fe) Lines Intensities

Table 6 shows the five iron lines, the 11 soil samples, and the percent change due to magnetic confinement of the integrated area of the spectral emission.

Table 6. Percent increase due to magnetic confinement of the Fe spectral lines.

Soil Sample	259.93 nm	273.96 nm	274.32 nm	274.69 nm	275.57 nm
GBW07013	144.23%	126.72%	82.41%	126.59%	135.08%
GBW07113	116.25%	115.20%	89.89%	112.56%	111.56%
GBW07311	42.82%	40.81%	35.48%	39.90%	39.96%
BCR2	18.84%	22.29%	28.17%	21.38%	7.13%
BHVO2	18.67%	20.38%	17.33%	20.17%	19.54%
AGV2	12.69%	12.44%	15.06%	11.14%	13.07%
GBW07110	15.41%	9.04%	17.83%	10.14%	11.44%
GBW07312	7.09%	9.19%	8.44%	9.61%	9.17%
JA1	-2.81%	-5.42%	-0.60%	-5.50%	-4.34%
JA2	-5.54%	-8.78%	-8.13%	-8.22%	-8.30%
GBW07104	-14.49%	-18.47%	-8.01%	-17.00%	-15.60%

Spectral intensities from the BHVO2 sample were enhanced under magnetic confinement, as shown in Figs. 14A and B. BHVO2 is an average sample based upon its reaction to magnetic confinement. BHVO2 is an average reaction to magnetic confinement as compared to the other samples. The yellow arrows point to the iron lines of interest, however, the other three spectral peaks shown in Fig 14B are also iron spectral lines.

A **B**

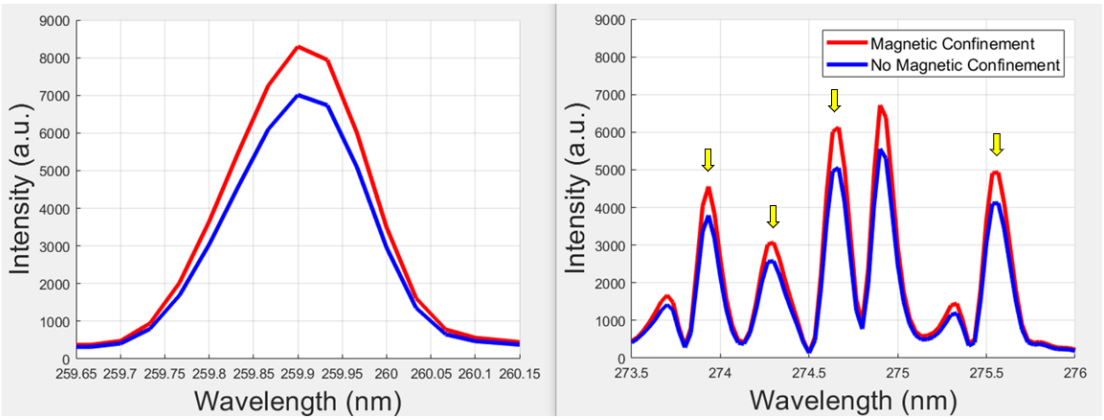

Figure 14. Spectral lines Fe II for sample BHVO2. (A) is the Fe II peak at 259.94 nm. (B) are the Fe II peaks at 273.955, 274. 32, 274.69, and 275.57 nm. The average increase in the integrated peak area was 19.21%.

BHVO2 has a large iron content at over 172,000 ppm. The five iron spectral lines without magnetic confinement enhancement are larger than other soil samples with smaller iron concentrations.

Unlike most samples tested, the spectral intensities from the GBW07104 sample shows no benefit due to magnetic confinement as shown in Fig. 15A and B. This is the first sample that has shown a disadvantage due to magnetic confinement. To ensure it was not an error, sample GBW07104 was tested a second time under magnetic confinement with similar negative results.

A **B**

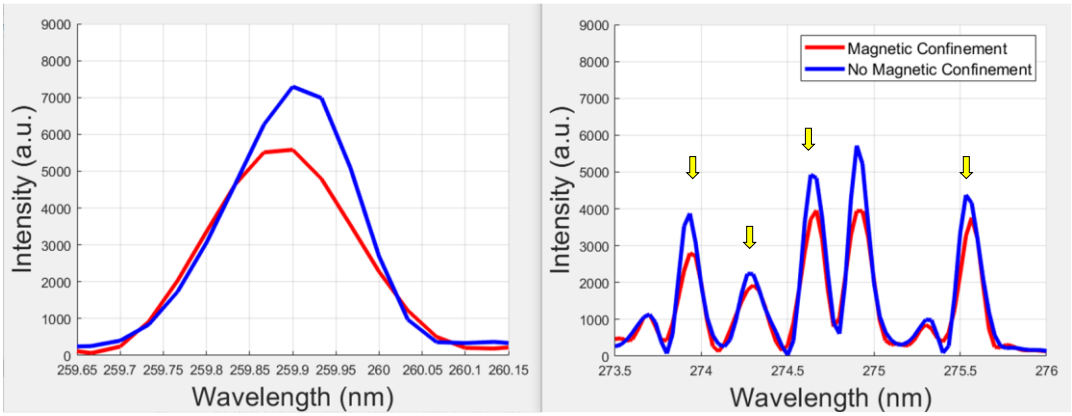

Figure 15. Spectral lines Fe II for sample GBW07104. (A) is the Fe II peak at 259.94 nm. (B) are the Fe II peaks at 273.955, 274. 32, 274.69, and 275.57 nm. The average decrease in the integrated peak area was 15.08%. This sample showed the most decrease because of magnetic confinement.

Sample GBWO7113 had one of the best reactions to magnetic confinement. The average spectral intensity increase was 111.62% as shown in Fig 16A and B. GBWO7113 has one of the lowest concentrations of iron at only 44,831 ppm. In comparison to the other soil samples, the five iron spectral lines without magnetic confinement enhancement are small as a result.

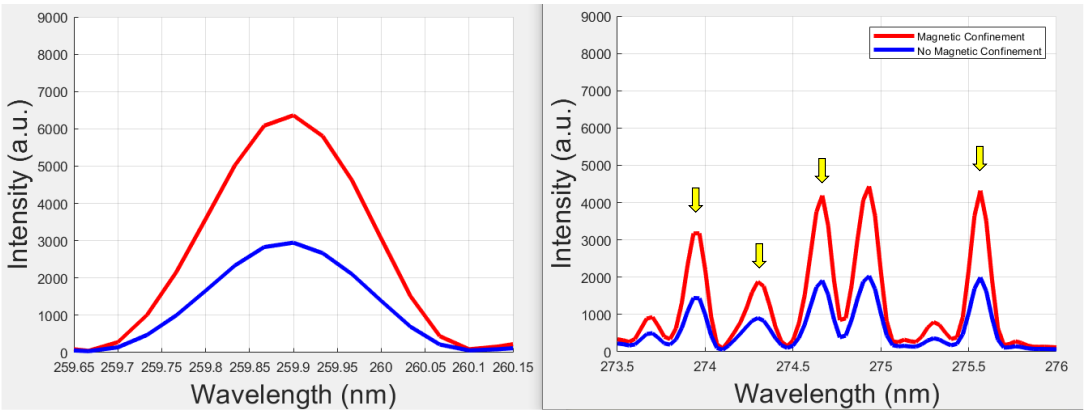

Figure 16. Spectral lines Fe II for sample GBW07113. (A) is the Fe II peak at 259.94 nm. (B) are the Fe II peaks at 273.955, 274. 32, 274.69, and 275.57 nm. The average increase in the integrated peak area was 111.62%.

4.2. Actinides

4.2.1 Uranium Spectral Lines

Uranium lines that were looked for based on previous studies [13,29,34,67,86], included U I 356.659 nm, U I 358.488 nm, U II 409.013 nm, U I 436.205 nm, U II 447.23 nm, U I 502.738 nm, U I 591.57 nm, and U I 682.691 nm. Table 7 shows the resolution of the uranium lines by soil sample. A fully resolved peak shows a gaussian curve that is statistically significant. A mostly resolved peak is not statistically significant and the peak's end points are overlapped with other spectral peaks. A partial peak is overlapped with other peaks, making one side of the peak unrecognizable. A partially resolved peak is more distorted than a mostly resolved peak.

Table 7. Uranium spectral line resolution by soil sample.

U neutral and ion	Atomic Line (nm)	7103 18.8 ppm	7311 9.1 ppm	7312 7.8 ppm	7113 4.83 ppm
Uranium I	356.66	not	not	not	not
Uranium I	358.49	partially	partially	partially	partially
Uranium I	367.01	partially	not	not	not
Uranium II	409.01	mostly	partially	not	partially
Uranium I	436.21	mostly	not	not	not
Uranium II	447.23	not	not	not	not
Uranium I	502.74	not	not	not	not
Uranium I	591.54	partially	not	not	not
Uranium I	682.69	not	not	not	not

The mostly resolved spectral peak of uranium at 436.21 nm is far from being statistically significant. Fig. 17A, B, and C show the 436.21 nm uranium line. Fig. 17A shows the macro of the magnetically confined spectral intensity. Fig. 17B shows the macro of the unconfined spectral intensity. Fig. 17C shows the micro of both the magnetically confined and unconfined spectral lines. The amount the magnetic confinement increased the spectral intensity cannot be quantified, because there is not an unconfined peak to base calculations.

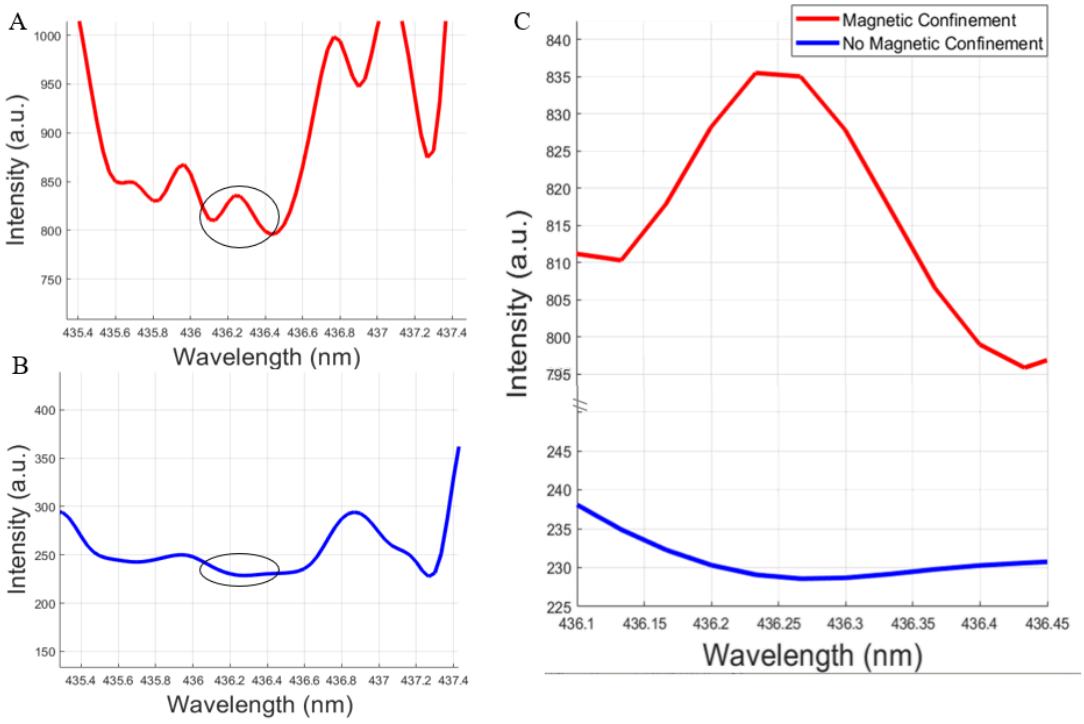

Figure 17. Uranium I line 436.21 nm of sample GBW07103. (A) is the macro of the magnetically confined line. (B) is the macro of the unconfined line. (C) is the micro of the two lines combined.

However, as shown in Fig. 18A and B, the amount the integrated area of the spectral emission line of uranium II at 409.01 nm increases because of magnetic confinement can be measured. The unconfined emission line has a slight peak at 409.01nm. The integrated area increased by 3.43 times under magnetic confinement. This peak is not statistically significant. The integrated area of the peak alone (I_A) was 25.05 and the area below the curve (I_B) was 409.2. Because I_A is not greater than 3x $\sqrt{I_B}$, the peak is not statistically significant. The reason why this peak is not statistically significant is that it did not rise

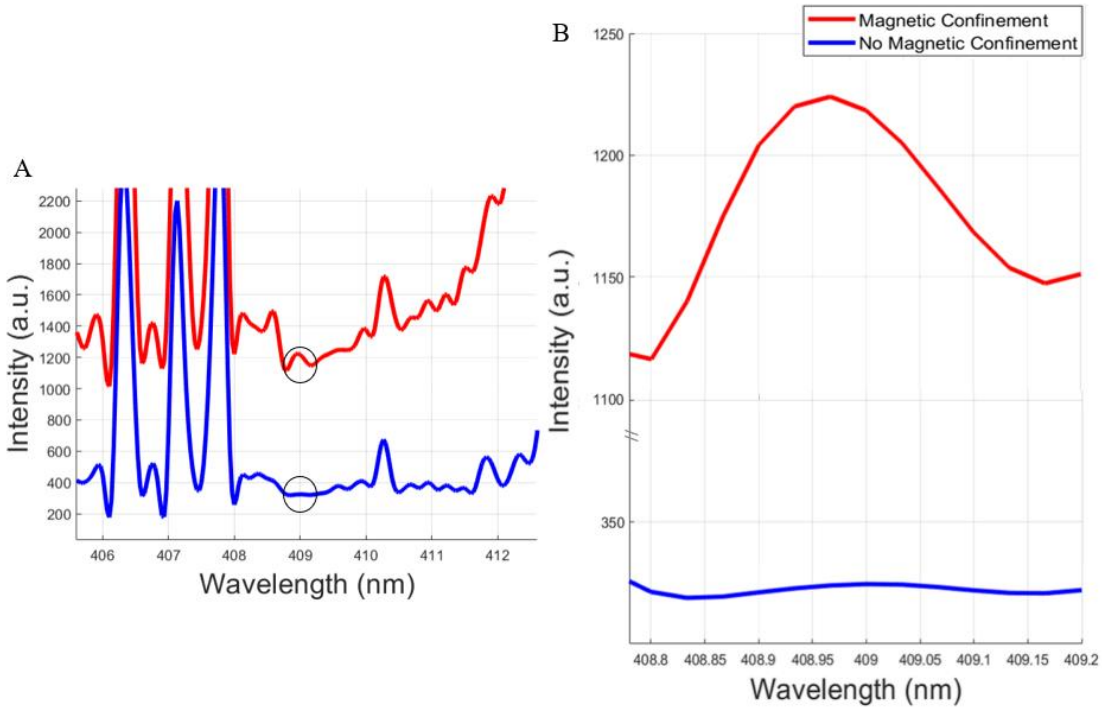

Figure 18. Uranium II line 409.01 nm of sample GBW07103. (A) is the macro of the spectral intensity lines. (B) is the micro of the U II spectral line.

high enough beyond its magnetically enhanced background. Even though the peak grew over 3x with magnetic confinement, the background grew even more. Had the magnetically

confined peak grown from near the same base as the iron lines did, then the peak could be shown to be statistically significant.

4.2.2 Thorium Spectral Lines

Thorium spectral lines were chosen based on their relative intensity from the NIST database [38]. Table 8 shows the selected spectral lines and the tested soil samples in descending order of thorium concentration. Like the uranium table, a fully resolved peak shows a gaussian curve that is statistically significant. A mostly resolved peak is not statistically significant and the peak's end points are overlapped with other spectral peaks. A partial peak is overlapped with other peaks making one side of the peak unrecognizable. A partially resolved peak is more distorted than a mostly resolved peak. As the data was being calculated, it became obvious that neither the of the observed spectral lines at 645.73

Table 8. Thorium spectral line resolution by soil sample.

Th neutral and ion	Atomic Line (nm)	7103 54 ppm	7113 27.1 ppm	7311 23.3 ppm	7312 21.4 ppm	7110 16.7 ppm	AGV2 6.1 ppm	BCR2 5.7 ppm	JA2 5 ppm	7104 2.6 ppm	BHVO2 1.22 ppm	JA1 0.76 ppm
Thorium I	395.04	not	not	not	not	not	not	not	not	not	not	not
Thorium II	422.67	not	not	not	not	not	not	not	not	not	not	not
Thorium I	572.02	partially	not	not	not	not	partially	not	not	not	not	not
Thorium I	576.06	mostly	not	not	not	not	not	not	not	not	not	not
Thorium I	618.26	not	not	not	not	not	not	not	not	not	not	not
Thorium I	645.73	partially	partially	partially	partially	partially	partially	partially	partially	partially	not	partially
Thorium I	658.39	not	not	not	not	not	not	not	not	not	not	not
Thorium I	691.12	fully	fully	fully	fully	fully	fully	mostly	partially	fully	not	partially
Thorium I	716.89	not	not	not	not	not	not	not	not	not	not	not
Thorium I	920.4	not	not	not	not	not	not	not	not	not	not	not
Thorium I	939.91	not	not	not	not	not	not	not	not	not	not	not

nm and 691.12 nm could have not been thorium lines, because theses spectral lines were observed in nearly all samples. Table 9 removes those two atomic lines and the samples that do not appear to have any thorium spectral emission peaks at the atomic lines studied.

Table 9. Thorium spectral line resolution without atomic lines 645.73 nm and 691.12 nm.

Th neutral and ion	Atomic Line (nm)	7103 54 ppm	AGV2 6.1 ppm
Thorium I	395.04	not	not
Thorium II	422.67	not	not
Thorium I	572.02	partially	partially
Thorium I	576.06	mostly	not
Thorium I	618.26	not	not
Thorium I	658.39	not	not
Thorium I	716.89	not	not
Thorium I	920.4	not	not
Thorium I	939.91	not	not

The mostly resolved spectral peak of thorium at 576.06 nm is not statistically significant. Fig. 19A and B show the 576.06 nm thorium line. Fig. 19A shows the macro

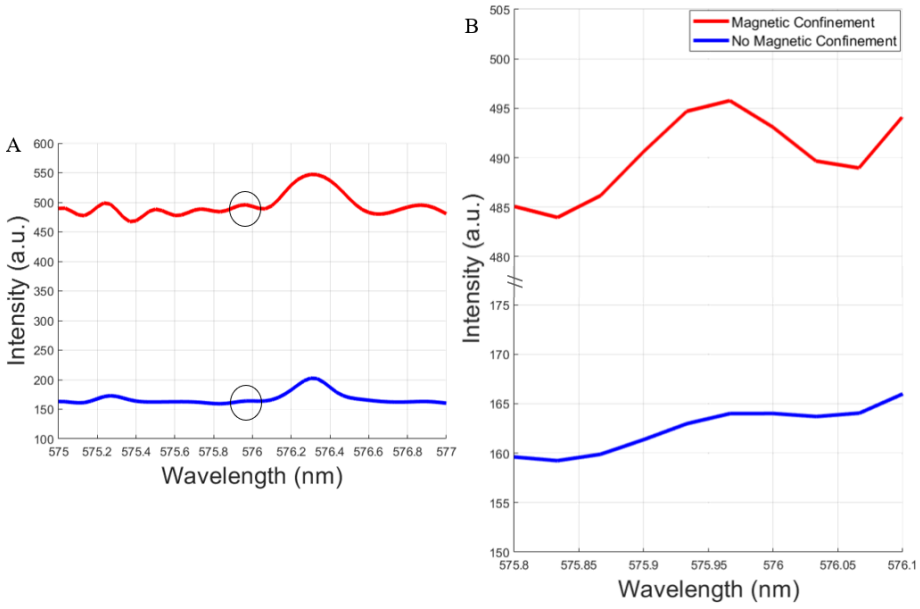

Figure 19. Thorium I line 576.06 nm of sample GBW07103. (A) is the macro of the spectral intensity lines. (B) is the micro of the Th I spectral line.

of the spectral intensity while Fig 19B shows the micro of the emission line.

From the AGV2 soil sample, a partially resolved peak of the thorium I spectral line at 572.02 nm is shown in Fig. 20.

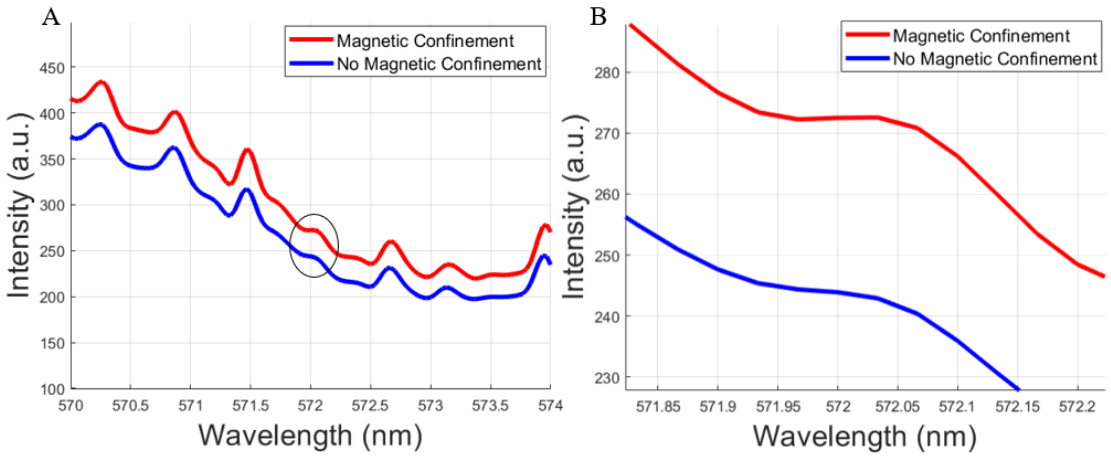

Figure 20. Thorium I line 572.02 nm of sample AGV2. (A) is the macro of the spectral intensity lines. (B) is the micro of the Th I spectral line.

4.2.3 Using the Ever-Bright Laser

After calibrating the Catalina Scientific Spectrograph and setting the Q switch delay to 190 microseconds, data was collected using two soil samples that had high concentrations of actinides when compared to the other samples. Their concentrations are still low, as shown in Table 8. Magnetic confinement increased the spectral intensity as shown in Fig 21. However, it appears more difficult to identify specific peaks, possibly due to being in ambient air and not in an argon environment. Looking for uranium and thorium spectral lines was problematic in this experiment due to the actinide's low concentration,

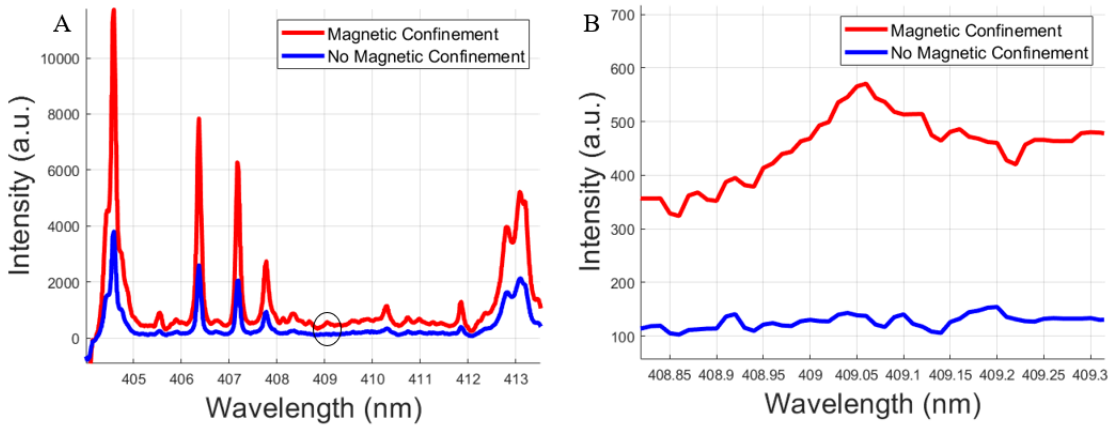

Figure 21. (A) Uranium II line 409.01 nm of sample GBW07311. (A) is the macro of the spectral intensity lines. (B) is the micro of the U II spectral line.

small spectral lines, and larger amount of background noise. Fig 21 shows the uranium spectral line at 409.01 nm going from the macro view of several peaks in Fig. 21A to the micro view of just the uranium II line. The magnetic confinement shows an increase in the spectral emission. The emission without magnetic confinement has no such increase in that same region. The integrated area of the uranium peak increased by 324% from the unconfined spectral intensity to the magnetically confined spectral intensity. This spectral line is large enough to be considered statistically significant because the area under the curve ($I_A + I_B$) minus the area below the curve (I_B) is larger than three times the square root of the area below the curve. For this spectral emission $I_A = 50.25$ and $I_B = 129$. The square root of three times $I_B = 34.07$, which is less than I_A. This is the same spectral line that was determined not be statistically significant with the HH-LIBS. The increase of the spectral intensity is due to the laser plume created from a more powerful laser and closer proximity of the magnets to the plasma plume.

4.3. Principal Component Analysis

Principal Component Analysis (PCA) provides a quantitative method to determine a correlation within the samples' elemental composition and their spectral intensity with and without magnetic confinement. PCA shows which elements create the most variance

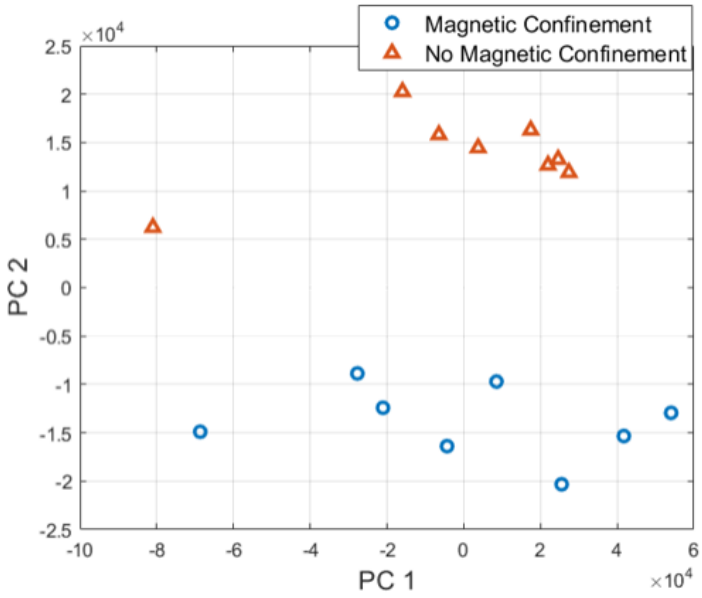

Figure 22. Principal Component 2 shows the separation between the magnetically confined test and the unconfined test of soil sample JA2.

between magnetically confined tests and unconfined tests. With most of the soil samples, magnetic confinement was a benefit to the spectral intensity. This was not the case with JA2. Fig. 22 shows the PCA of the soil sample JA2. The elements that are in principle component two are causing the separation of the magnetically confined test from the unconfined test. Principle component one has more variance, therefore, a greater spread of the test. Principle component two is more interesting.

The loadings for principal component two show several atomic lines that contribute to the high variance between the magnetically confined test and the unconfined test as shown in Fig. 23. For soil sample JA2, the most variance comes from Co II found at 280.17nm, V II found at 279.43 nm, Cr II or Fe II found at 251.66 nm, and Fe I found at 588.88 nm. The cobalt lines may give insight to the negative response to magnetic confinement since cobalt

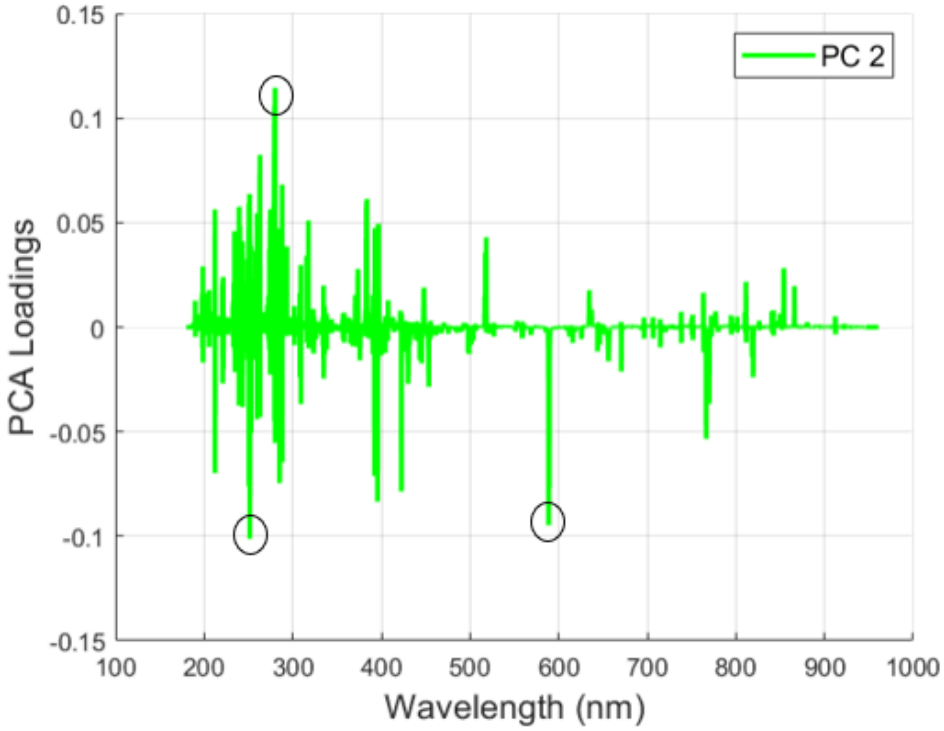

Figure 23. Principal Component 2 showed the most variance with respect to magnetic containment. In sample JA2, the largest PC2 Loadings are Co II, V II, Cr II or Fe I and Fe I.

has been shown to have an adverse reaction to magnetic confinement [77]. JA2 did the worst of the tested samples when looking at the entire spectrum. Correlating the benefit that the magnetic field had on the soil samples to the quantity of cobalt, iron, chromium, and vanadium shows that they all indeed have a negative correlation as shown in Table 10.

This is not a strong negative correlation. The greater the spectral intensity signal boosts of a soil sample, the smaller the quantity of these four elements will be. The quantity of iron in the soil samples averages 91,575 ppm. It is easy to see why iron would influence the magnetic confinement tests. However, cobalt, vanadium, and chromium are all trace

Table 11. Negative correlating elements.

Average % Increase	r
Cobalt	-0.54
Iron	-0.41
Vanadium	-0.35
Chromium	-0.31

elements having a sum of about 200 ppm depending on the sample. The results of the PCA show that the variance between magnetically confined tests and magnetically unconfined tests is a result of the elements cobalt, vanadium, and chromium, as shown in Fig. 23. It is causation because the PCA showed that the trace elements showed the most variance between the magnetically confined tests and the unconfined tests. These trace elements and iron caused the variance. The correlation between magnetic confinement and the trace elements is also causation. The correlation is supported by the results of the PCA.

A fair sample was GBW07312. It had the small increase in integrated area due to magnetic confinement for the entire spectrum and for the five iron lines of only 8.45%. Fig. 24 shows the PCA of the soil sample GBW07312. Like JA2, principal component two is more interesting than principal component one. As shown in Fig. 25, there are four

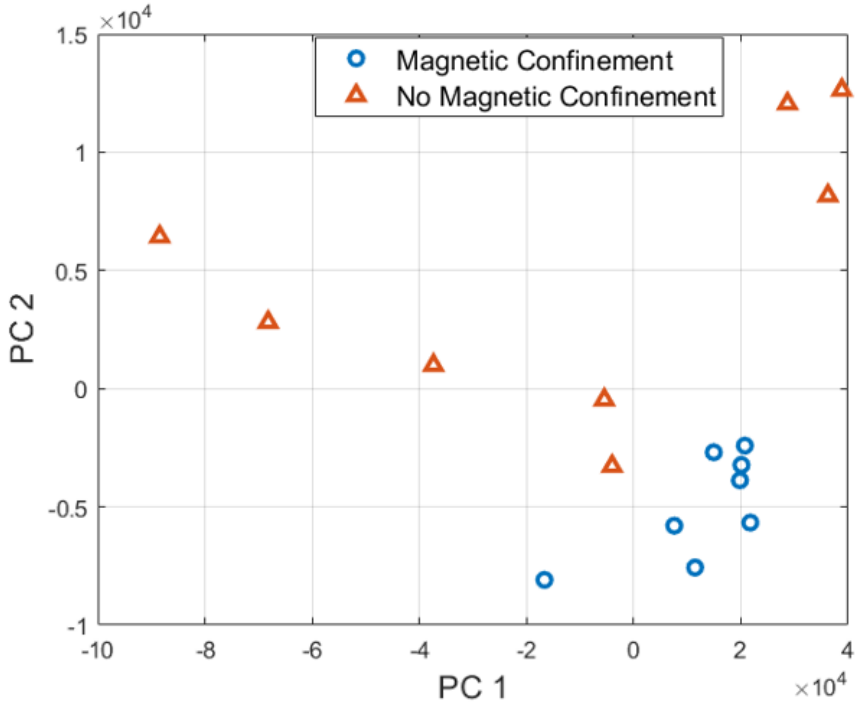

Figure 24. Principal Component 2 shows the separation between the magnetically confined tests and the unconfined tests more so than PC1 in soil sample GBW07312.

atomic lines that contribute to the variance in PC 2. The first spectral line is located at 292.93 nm. It may be Fe I or Th I. There are several elements that could be associated with atomic line 396.53 nm. It may be Co I, Zr III, or Zn I. A third spectral line, 393.26 nm, is a Fe I line, and a fourth spectral line, 396.13 nm, is a C I line. This sample does have carbon but not every sample has a recorded quantity of carbon. For the samples that have carbon, there is a strong negative correlation of r = -0.81 of carbon to the spectral increase, due to magnetic confinement.

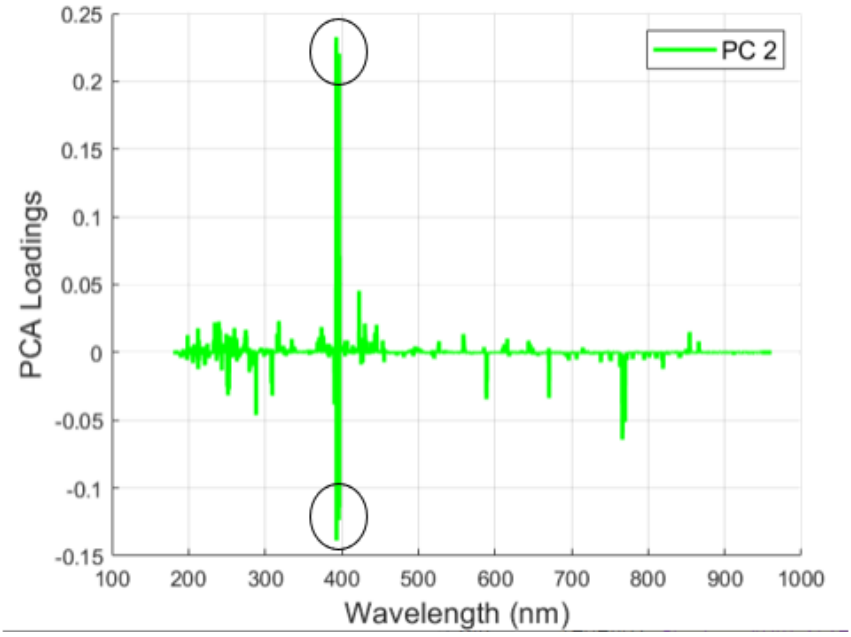

Figure 25. Principal Component 2 showed the most variance with respect to magnetic containment. In sample GBW07312, the largest PC 2 Loadings are C I, Fe I, Th I or Fe I, and Co I or Zr III or Zn I.

Even though PC 2 shows the largest difference between the magnetically confined tests and the unconfined tests, PC 1 should give insight as to why the magnetic confined tests are clustered on the PC 1 axis. As shown in Fig. 26, PC 1 is composed of Pr and Dy. These two elements create the most variance between the tests. From Fig. 24, most of the magnetically confined tests are grouped to the right, while the unconfined tests have a greater spread but are more weighted to the left. There is less than 12 ppm of these elements combined. If this small of a quantity could cause this variance, a larger quantity of these elements may show a more uniform split between the magnetically confined and unconfined tests.

Magnetic confinement had a strong positive effect on soil sample GBW07113. Unlike the previous two samples, PC 1 shows a greater effect on the variance between the magnetically confined tests and the unconfined tests as shown in Fig 27. However, PC 2

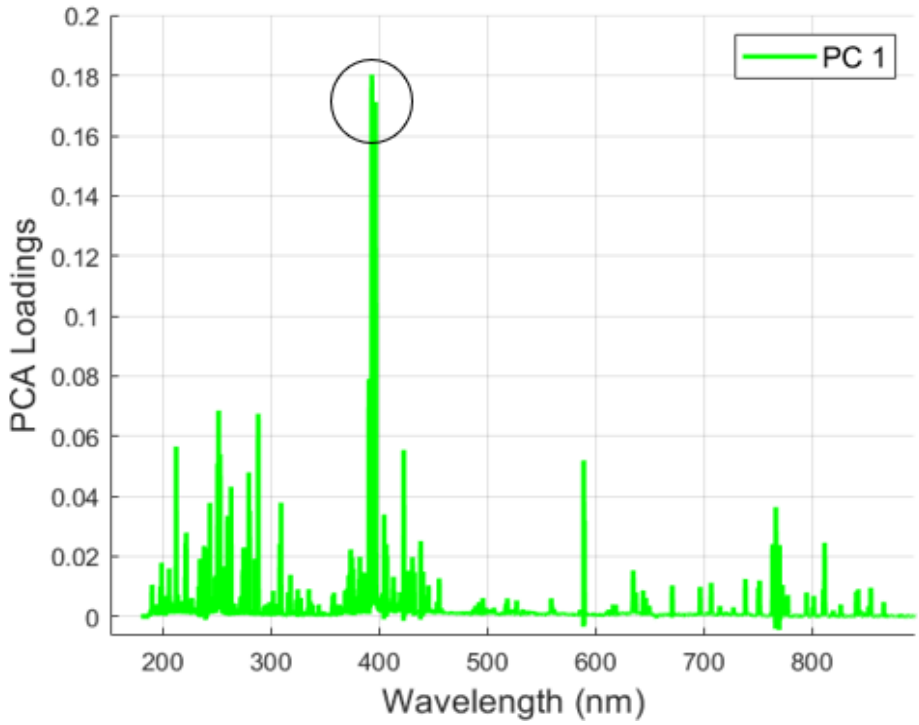

Figure 26. Soil sample GBW07312 PC 1's atomic lines are Pr II 396.66 nm and Dy II 393.15 nm.

does show some separation with respect to magnetic confinement. Fig. 28A shows two atomic lines that are displayed to have the most variance in PC 1. They are Pr II 396.66 nm and Dy II 393.15. Fig. 28B shows six atomic lines that are displayed to have the most variance in PC 2. There are four thorium lines, a sodium line, an aluminum line, and a dysprosium line.

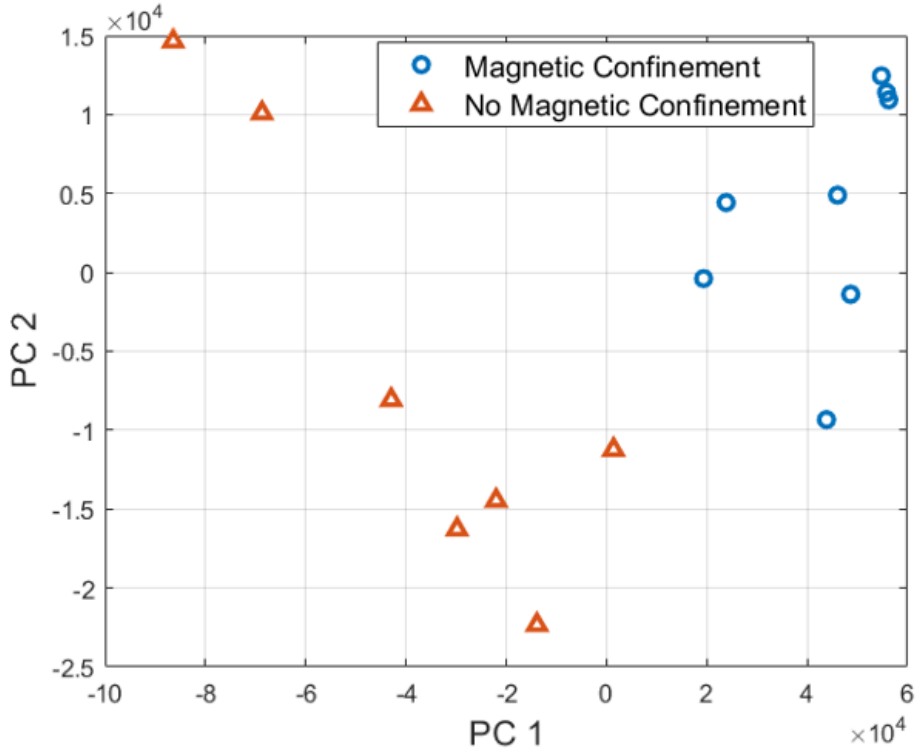

Figure 27. Principal Component 1 shows the separation between the magnetically confined test and the unconfined test more so than PC2 in soil sample GBW07113.

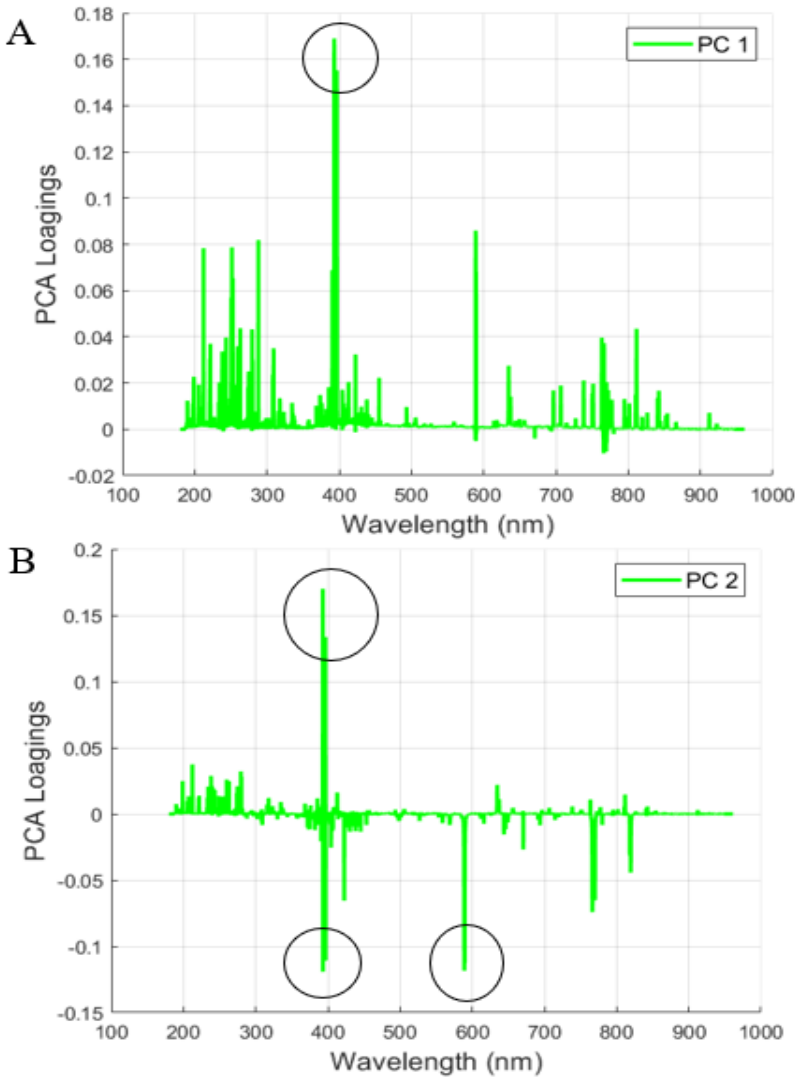

Figure 28. Principal Components for soil sample 7113. (A) PC 1 has Pr II 396.66 nm and Dy II 393.15 nm. (B) PC 2 has seven atomic lines. Na I 393.06, Th II 393.33, Al 396.15 nm, Th I 396.63, Dy II 396.83, Th I 589.06 nm, and Th I 489.63 nm.

As shown in Table 11, the Pearson coefficient, r value, of the spectral intensity of the five iron lines of the eleven samples with the principal components trace elements of dysprosium, thorium, and praseodymium in those soil samples. There is a strong positive correlation of r = 0.9 between dysprosium and increasing the spectral intensity of the

studied iron lines. The Pearson coefficient is r = 0.92 for the sum of the three elements Dy, Th, and Pr. Fig. 29 shows a high positive correlation between the sum of the trace elements Dy, Th, and Pr and the percent of spectral emission intensity increase due to magnetic confinement. There is a positive correlation between the lanthanides and actinides in the

Table 11. Positive correlating elements.

Average % Increase	r
Dysprosium	0.90
Thorium	0.87
Praseodymium	0.78

soil samples and the increase of spectral emission intensity due to magnetic confinement. Elements were also combined based on being magnetic, non-magnetic, and para magnetic.

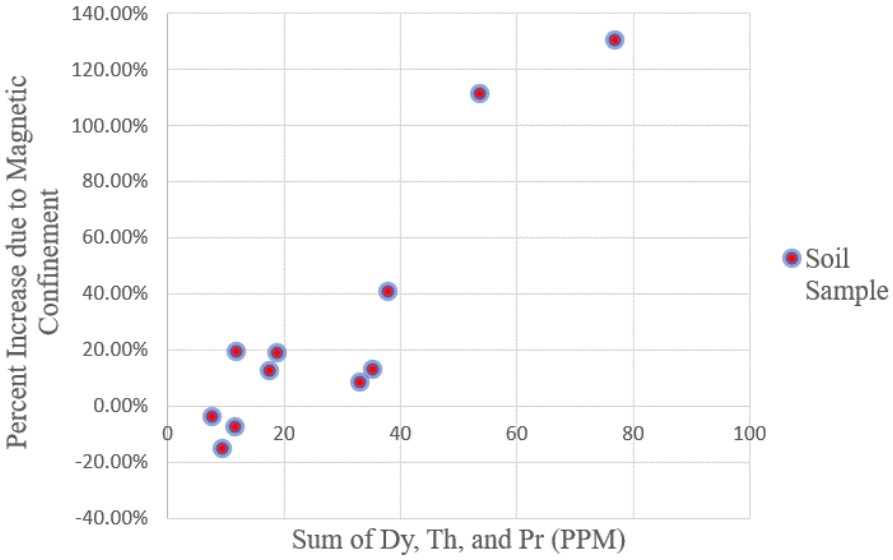

Figure 29. Sum of Dy, Th, and Pr verses the percent of spectral emission intensity increase due to magnetic confinement.

None of these combinations had a strong positive or negative correlation to the magnetic spectral intensity boost. Greater correlation was found from randomly combining elements.

Fig. 30 shows the similarities between Fe in Fig. 30A and the trace elements Co and V in Fig. 30B. The sum of the three elements were not combined due to the quantity of Fe, which was three orders of magnitude greater than Co and V.

Several correlations can be made between the elemental composition of the soil samples and the effect of magnetic confinement. For example, summing the lanthanides

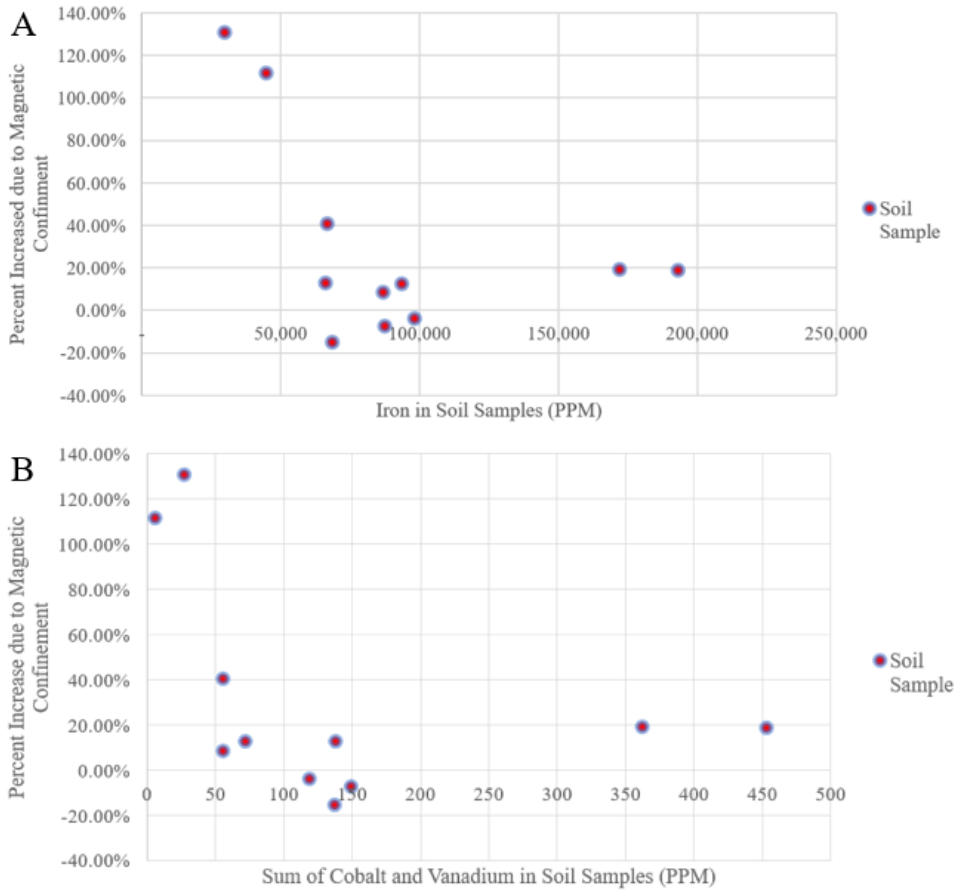

Figure 30. (A) Fe and (B) Co and V have negative correlations to the percent of spectral emission intensity increase due to magnetic confinement.

and actinides together with scandium and yttrium from group IIIB has a high correlation of r =0.90 to the increase of the integrated area of the spectral emission intensity. However, a high correlation does not guarantee causation. There was not a strong negative correlation of r < -0.80, with any of the combinations of magnetic, paramagnetic, and nonmagnetic elements. The closest combination of elements was Al, C, Fe, Mn, Mg, Na, and Ti which gave a Pearson coefficient of r = -0.53. The sum of these seven elements make up 20% of the soil samples on average and has no greater negative correlation than the trace element cobalt.

.

Chapter 5: Conclusions

5.1. Magnetic Confinement Apparatus for HH-LIBS

The purpose of this research was to develop an apparatus for a HH-LIBS device that would amplify the intensity of iron, thorium, and uranium spectral lines through magnetic confinement. In particular, the goal was to develop an apparatus that was easy to use and adjustable so it could be used with other manufactured HH-LIBS. Current collection methods following a nuclear incident lack the ability to rapidly identify the collected material's elemental composition. Previous research has demonstrated the benefits of magnetic confinement using benchtop LIBS, however, a benchtop LIBS is not portable, nor would it be practical in an austere environment following a nuclear incident. Previous research has also shown several ways to increase the spectral intensity of LIBS, but only magnetic confinement can be used immediately with a Commercial Off -The-Shelf (COTS) HH-LIBS without any modifications to the HH-LIBS.

This research used a Z-300 HH-LIBS with certified soil samples from Los Alamos National Laboratory, and several permanent neodymium magnets. After many tests with magnet placement, an initial wooden prototype was built. The test with the Everbright Laser gave better results due to being a more powerful laser that created a lager plasma plume and a lager magnetic field from the manipulation of the magnetic containment apparatus.

5.2. Principal Component Analysis

Using the magnetic confinement apparatus, five iron lines were studied along with nine uranium lines and 19 thorium lines. Though magnetic confinement for many of the

soil samples increased the spectral intensity, some of the spectral intensities decreased under magnetic confinement. Using PCA, dysprosium and praseodymium were shown to have the greatest positive effect on the spectral intensity due to magnetic confinement, while iron, cobalt, and vanadium were shown to have a negative effect on the spectral intensity due to magnetic confinement.

5.3. Benefits of Magnetic Confinement

In this study magnetic confinement has shown that it can increase the integrated spectral intensity by over 2x. Therefore, trace elements that are in smaller quantities will be magnified. The average increase of spectral emission intensity due to magnetic confinement in the five iron lines was 18.58%. Thorium atomic lines were shown to have increased emission intensity due to magnetic confinement. Soil samples with quantities as low as 4.83 ppm of uranium were shown to have increased emission intensity due to magnetic confinement.

5.4. Conclusions

From this research with the magnetic confinement apparatus and HH-LIBS, actinides can be accurately measured at a greater distance from a nuclear incident. Not only will this help analyze components from a nuclear event, but it will provide information to DoE, local officials, military leadership, and emergency response personnel.

From this research, uranium spectral lines were found at levels below their previous limits of detection as low as 158 ppm [34]. This technique can be used by the military to discern actinides. Industries can use this technique to detect trace elements in metals that

would otherwise be unable to find. The Food and Drug Administration testing would benefit from this technique to discover trace and heavy elements in food and drug products to ensure these elements are not above acceptable consumer levels.

5.5. Recommendations for Future Work

Follow-on research with the magnetic containment apparatus and HH-LIBS should focus on the effects of doping soil samples with dysprosium, thorium, and praseodymium to increase the intensity of spectral emissions under magnetic confinement. Not only are Dy, Th, and Pr highly correlated to the increase of spectral emission intensity from magnetic confinement, but Dy, Th, and Pr were shown to have greatest impact on the variance between magnetically confined test and unconfined test. Dy, Th, and Pr doping is worth future study.

REFERENCES

1. "National Technical Nuclear Forensics Ground Collection Team Standing Operating Procedures," (2020).

2. B. T. Manard, E. M. Wylie, and S. P. Willson, "Analysis of Rare Earth Elements in Uranium Using Handheld Laser-Induced Breakdown Spectroscopy (HH LIBS)," Appl. Spectrosc. **72**, 1653–1660 (2018).

3. R. Gaudiuso, M. Dell'Aglio, O. de Pascale, G. S. Senesi, and A. de Giacomo, "Laser induced breakdown spectroscopy for elemental analysis in environmental, cultural heritage and space applications: A review of methods and results," Sensors **10**, 7434–7468 (2010).

4. S. Petersen and A. Petersen, "Rare Earth Metals," https://periodictablegroups.wordpress.com/.

5. N. Connor, "Personal Dosimeter," https://www.personal-dosimeter.com/.

6. Y. Li, D. Tian, Y. Ding, G. Yang, K. Liu, C. Wang, and X. Han, "A review of laser-induced breakdown spectroscopy signal enhancement," Appl. Spectrosc. Rev. **53**, 1–35 (2018).

7. V. I. Babushok, F. C. DeLucia, J. L. Gottfried, C. A. Munson, and A. W. Miziolek, "Double pulse laser ablation and plasma: Laser induced breakdown spectroscopy signal enhancement," Spectrochim. Acta - Part B At. Spectrosc. **61**, 999–1014 (2006).

8. O. A. Nassef and H. E. Elsayed-Ali, "Spark discharge assisted laser induced breakdown spectroscopy," Spectrochim. Acta - Part B At. Spectrosc. **60**, 1564–1572 (2005).

9. S. J. Choi, K. J. Lee, and J. J. Yoh, "The laser-induced plasma persistence time extension in low pressures using the ablated mass confinement method," Spectrochim. Acta - Part B At. Spectrosc. **97**, 113–117 (2014).

10. Y. Li, C. Hu, H. Zhang, Z. Jiang, and Z. Li, "Optical emission enhancement of laser-produced copper plasma under a steady magnetic field," Appl. Opt. **48**, 105–110 (2009).

11. J. E. B. Ii, S. M. Clegg, L. A. Le, and L. N. Lopez, *Development of Laser Induced Breakdown Spectroscopy Instrumentation for Safeguards Applications* (2010), Vol. 836.

12. L. A. Le James E. Barefield II, Samuel M. Clegg, D. Kirk Veirs, Mike Browne, Leon N. Lopez, "Application of Laser Induced Breakdown Spectroscopy (LlBS) Instrumentation for International Safeguards," Proc. 10th Bienn. Conf. Eng. Syst. Des. Anal. ESDA 10 July 12-14, 2010, Istanbul, Turkey ESDA2010-24598 **836**, 1–4 (2001).

13. G. S. Senesi, R. S. Harmon, and R. R. Hark, "Field-portable and handheld laser-induced breakdown spectroscopy: Historical review, current status and future prospects," Spectrochim. Acta - Part B At. Spectrosc. **175**, 106013 (2021).

14. K. Y. Yamamoto, D. A. Cremers, M. J. Ferris, and L. E. Foster, "Detection of metals in the environment using a portable laser-induced breakdown spectroscopy instrument," Appl. Spectrosc. **50**, 222–233 (1996).

15. J. Cuñat, F. J. Fortes, L. M. Cabaĺin, F. Carrasco, M. D. Simón, and J. J. Laserna, "Man-portable laser-induced breakdown spectroscopy system for in situ characterization of karstic formations," Appl. Spectrosc. **62**, 1250–1255 (2008).

16. R. C. Wiens, S. Maurice, B. Barraclough, M. Saccoccio, W. C. Barkley, J. F. Bell, S. Bender, J. Bernardin, D. Blaney, J. Blank, M. Bouyé, N. Bridges, N. Bultman, P. Caïs, R. C. Clanton, B. Clark, S. Clegg, A. Cousin, D. Cremers, A. Cros, L. Deflores, D. Delapp, R. Dingler, C. D'Uston, M. Darby Dyar, T. Elliott, D. Enemark, C. Fabre, M. Flores, O. Forni, O. Gasnault, T. Hale, C. Hays, K. Herkenhoff, E. Kan, L. Kirkland, D. Kouach, D. Landis, Y. Langevin, N. Lanza, F. Larocca, J. Lasue, J. Latino, D. Limonadi, C. Lindensmith, C. Little, N. Mangold, G. Manhes, P. Mauchien, C. McKay, E. Miller, J. Mooney, R. V. Morris, L. Morrison, T. Nelson, H. Newsom, A. Ollila, M. Ott, L. Pares, R. Perez, F. Poitrasson, C. Provost, J. W. Reiter, T. Roberts, F. Romero, V. Sautter, S. Salazar, J. J. Simmonds, R. Stiglich, S. Storms, N. Striebig, J. J. Thocaven, T. Trujillo, M. Ulibarri, D. Vaniman, N. Warner, R. Waterbury, R. Whitaker, J. Witt, and B. Wong-Swanson, "The ChemCam instrument suite on the Mars Science Laboratory (MSL) rover: Body unit and combined system tests," Space Sci. Rev. **170**, 167–227 (2012).

17. R. Wiens, "Mars Curiosity Rover," available: https://mars.nasa.gov/msl/spacecraft/instruments/chemcam/.

18. "B&W Tek Handheld LIBS Analyzer for the Pharmaceutical Industry," https://bwtek.com/products/nanolibs/.

19. PI Consulting, "HITACHI VULCAN HANDHELD METAL ANALYZER," https://verichek.net/product/hitachi-vulcan-handheld-metal-analyzer.

20. B. Connors, A. Somers, and D. Day, "Application of Handheld Laser-Induced Breakdown Spectroscopy (LIBS) to Geochemical Analysis," Appl. Spectrosc. **70**, 810–815 (2016).

21. D. Day, B. Connors, M. Jennings, J. Egan, K. Derman, P. Soucy, S. Moller, and D. Sackett, "A full featured handheld LIBS analyzer with early results for defense and security," Next-Generation Spectrosc. Technol. VIII **9482**, 948206 (2015).

22. K. R. Price, "A Review of Transuranic Elements in Soils, Plants, and Animals," J. Environ. Qual. **2**, 62–66 (1973).

23. J. H. Hendry, S. L. Simon, A. Wojcik, M. Sohrabi, W. Burkart, E. Cardis, D.

Laurier, M. Tirmarche, and I. Hayata, "Human exposure to high natural background radiation: What can it teach us about radiation risks?," J. Radiol. Prot. **29**, (2009).

24. M. Thorne, "Background radiation: natural and man-made," J. Radiol. Prot. (2003).

25. N. Vajda, A. Törvényi, G. Kis-Benedek, C. K. Kim, B. Bene, and Z. Mácsik, "Rapid method for the determination of actinides in soil and sediment samples by alpha spectrometry," Radiochim. Acta **97**, 395–401 (2009).

26. Z. X. Lin, L. M. Liu, and L. W. Liu, "Validation of the solidifying soil process using laser-induced breakdown spectroscopy," Opt. Laser Technol. **83**, 13–15 (2016).

27. S. C. Jantzi, V. Motto-Ros, F. Trichard, Y. Markushin, N. Melikechi, and A. De Giacomo, "Sample treatment and preparation for laser-induced breakdown spectroscopy," Spectrochim. Acta - Part B At. Spectrosc. **115**, 52–63 (2016).

28. H. Xia and M. C. M. Bakker, "Single-shot LIBS spectral quality for waste particles in open air," Tech. Mess. **82**, 606–615 (2015).

29. R. C. Chinni, D. A. Cremers, L. J. Radziemski, M. Bostian, and C. Navarro-Northrup, "Detection of Uranium Using Laser-Induced Breakdown Spectroscopy," Appl. Spectrosc. **63**, 1238–1250 (2009).

30. B. A. Palmer, R. A. Keller, and R. Engleman, "An Atlas of Uranium Emission Intensities in A Hollow Cathode Discharge," (1980).

31. D. W. Steinhaus, L. J. Radziemski, R. D. Cowan, J. Blaise, G. Guelachvili, Z. Ben Osman, and J. Verges, *Present Status of the Analyses of the First and Second Spectra of Uranium (U I and U II) as Derived from Measurements of Optical Spectra* (1971).

32. Z. Hao, L. Guo, C. Li, M. Shen, X. Zou, X. Li, Y. Lu, and X. Zeng, "Sensitivity improvement in detection of V and Mn elements in steel using laser-induced breakdown spectroscopy with ring-magnet confinement," J. Mater. Chem. C **3**, 10715–10722 (2014).

33. C. Li, X. Gao, Q. Li, C. Song, and J. Lin, "Spectral enhancement of laser-induced breakdown spectroscopy in external magnetic field," Plasma Sci. Technol. **17**, 919–922 (2015).

34. Y. S. Kim, B. Y. Han, H. S. Shin, H. D. Kim, E. C. Jung, J. H. Jung, and S. H. Na, "Determination of uranium concentration in an ore sample using laser-induced breakdown spectroscopy," Spectrochim. Acta - Part B At. Spectrosc. **74**–**75**, 190–193 (2012).

35. A. Arshad, S. Bashir, A. Hayat, M. Akram, A. Khalid, N. Yaseen, and Q. S. Ahmad, "Effect of magnetic field on laser-induced breakdown spectroscopy of

graphite plasma," Appl. Phys. B Lasers Opt. **122**, (2016).

36. Q. Xiao, R. Hai, H. Ding, A. Huber, V. Philipps, N. Gierse, and G. Sergienko, "In-situ analysis of the first wall by laser-induced breakdown spectroscopy in the TEXTOR tokamak: Dependence on the magnetic field strength," J. Nucl. Mater. **463**, 911–914 (2015).

37. V. N. Rai, A. K. Rai, F.-Y. Yueh, and J. P. Singh, "Optical emission from laser-induced breakdown plasma of solid and liquid samples in the presence of a magnetic field," Appl. Opt. **42**, 2085 (2003).

38. "NIST Atomic Spectra Database," https://physics.nist.gov/PhysRefData/ASD/lines_form.html.

39. scikit-learn developers, "User Guide SciAps Z-200 and Z-300 Handheld LIBS Analyzers," SciAps 1–50 (2020).

40. L. B. Guo, W. Hu, B. Y. Zhang, X. N. He, C. M. Li, Y. S. Zhou, Z. X. Cai, X. Y. Zeng, and Y. F. Lu, "Enhancement of optical emission from laser-induced plasmas by combined spatial and magnetic confinement," Opt. Express **19**, 14067 (2011).

41. N. Taylor, *LASER: The Inventor, the Nobel Laureate, and the Thirty-Year Patent War*. (Simon &Schuster, 2000).

42. L. J. Radziemski, "From LASER to LIBS, the path of technology development," Spectrochim. Acta - Part B At. Spectrosc. **57**, 1109–1113 (2002).

43. L. Radziemski and D. Cremers, "A brief history of laser-induced breakdown spectroscopy: From the concept of atoms to LIBS 2012," Spectrochim. Acta - Part B At. Spectrosc. **87**, 3–10 (2013).

44. D. A. Cremers and R. C. Chinni, "Laser-induced breakdown spectroscopy-capabilities and limitations," Appl. Spectrosc. Rev. **44**, 457–506 (2009).

45. D. Cremers and L. Radziemski, *Handbook of Laser-Induced* (2013).

46. M. Pérez-Rodríguez, P. M. Dirchwolf, T. V. Silva, A. L. Vieira, J. A. G. Neto, R. G. Pellerano, and E. C. Ferreira, "Fast spark discharge-laser-induced breakdown spectroscopy method for rice botanic origin determination," Food Chem. **331**, (2020).

47. J. P. Singh and S. N. Thakur, *Laser-Induced Breakdown Spectroscopy*, First edit (2007).

48. F. Anabitarte and A. Cobo, "Laser-Induced Breakdown Spectroscopy : Fundamentals , Applications , and Challenges," **2012**, (2012).

49. J. El Haddad, L. Canioni, and B. Bousquet, "Good practices in LIBS analysis: Review and advices," Spectrochim. Acta - Part B At. Spectrosc. **101**, 171–182 (2014).

50. J. Rakovský, P. Čermák, O. Musset, and P. Veis, "A review of the development of portable laser induced breakdown spectroscopy and its applications," Spectrochim. Acta - Part B At. Spectrosc. **101**, 269–287 (2014).

51. M. L. Najarian and R. C. Chinni, "Temperature and electron density determination on Laser-Induced Breakdown Spectroscopy(LIBS) plasmas: A physical chemistry experiment," J. Chem. Educ. **90**, 244–247 (2013).

52. Z. Wang, L. Li, L. West, Z. Li, and W. Ni, "Spectrum standardization for laser-induced breakdown spectroscopy measurements 1 Introduction," (n.d.).

53. B. Kearton and Y. Mattley, "Laser-induced breakdown spectroscopy: Sparking new applications," Nat. Photonics **2**, 537–540 (2008).

54. L. B. Guo, Z. Q. Hao, M. Shen, W. Xiong, X. N. He, Z. Q. Xie, M. Gao, X. Y. Li, X. Y. Zeng, and Y. F. Lu, "Accuracy improvement of quantitative analysis by spatial confinement in laser-induced breakdown spectroscopy," Opt. Express **21**, 18188 (2013).

55. C. Gautier, P. Fichet, D. Menut, and J. Dubessy, "Applications of the double-pulse laser-induced breakdown spectroscopy (LIBS) in the collinear beam geometry to the elemental analysis of different materials," Spectrochim. Acta - Part B At. Spectrosc. **61**, 210–219 (2006).

56. A. Bogaerts, Z. Chen, and D. Autrique, "Double pulse laser ablation and laser induced breakdown spectroscopy: A modeling investigation," Spectrochim. Acta - Part B At. Spectrosc. **63**, 746–754 (2008).

57. X. Mao, X. Zeng, S. B. Wen, and R. E. Russo, "Time-resolved plasma properties for double pulsed laser-induced breakdown spectroscopy of silicon," in *Spectrochimica Acta - Part B Atomic Spectroscopy* (2005), Vol. 60, pp. 960–967.

58. I. Y. Elnasharty, F. R. Doucet, J. F. Y. Gravel, P. Bouchard, and M. Sabsabi, "Double-pulse LIBS combining short and long nanosecond pulses in the microjoule range," J. Anal. At. Spectrom. **29**, 1660–1666 (2014).

59. X. Jiang, P. Hayden, J. T. Costello, and E. T. Kennedy, "Double-pulse laser induced breakdown spectroscopy with ambient gas in the vacuum ultraviolet: Optimization of parameters for detection of carbon and sulfur in steel," Spectrochim. Acta - Part B At. Spectrosc. **101**, 106–113 (2014).

60. V. Piñon, C. Fotakis, G. Nicolas, and D. Anglos, "Double pulse laser-induced breakdown spectroscopy with femtosecond laser pulses," Spectrochim. Acta - Part B At. Spectrosc. **63**, 1006–1010 (2008).

61. M. E. Asgill, M. S. Brown, K. Frische, W. M. Roquemore, and D. W. Hahn, "Double-pulse and single-pulse laser-induced breakdown spectroscopy for distinguishing between gaseous and particulate phase analytes," Appl. Opt. **49**, (2010).

62. R. Noll, R. Sattmann, V. Sturm, and S. Winkelmann, "Space- and time-resolved dynamics of plasmas generated by laser double pulses interacting with metallic samples," J. Anal. At. Spectrom. **19**, 419–428 (2004).

63. B. Rashid, R. Ahmed, R. Ali, and M. A. Baig, "A comparative study of single and double pulse of laser induced breakdown spectroscopy of silver," Phys. Plasmas **18**, (2011).

64. M. J. Kushner, R. D. Milroy, and W. D. Kimura, "A laser-triggered spark gap model," J. Appl. Phys. **58**, 2988–3000 (1985).

65. W. Zhou, K. Li, Q. Shen, Q. Chen, and J. Long, "Optical emission enhancement using laser ablation combined with fast pulse discharge," Opt. Express **18**, 2573 (2010).

66. L. I. Kexue, W. Zhou, Q. Shen, J. Shao, and H. Qian, "Signal enhancement of lead and arsenic in soil using laser ablation combined with fast electric discharge," Spectrochim. Acta - Part B At. Spectrosc. **65**, 420–424 (2010).

67. Y. F. Lu, X. K. Shen, and H. Ling, "Laser-induced Breakdown Spectroscopy Combined with Spatial Confinement of Plasmas and Laser-induced Fluorescence for Trace-Materials Detection," 1–8 (2016).

68. Z. Yin, Hualiang; Hou, Zongyu; Yuan, Tingbi; Wang, Zhe; Ni, Weidou; Li, "Application of spatial confinement for gas analysis using laser-induced breakdown spectroscopy to improve signal stability Bowl-shaped confinement was designed to increase signal stability by stabilizing the core of plasma and confining plasma energy in a," J. Anal. At. Spectrom. (2014).

69. Y. Wang, A. Chen, L. Sui, S. Li, D. Liu, X. Wang, Y. Jiang, X. Huang, and M. Jin, "Persistence of atomic spectral line on laser-induced Cu plasma with spatial confinement," Phys. Plasmas **23**, (2016).

70. A. M. Popov, F. Colao, and R. Fantoni, "Enhancement of LIBS signal by spatially confining the laser-induced plasma," J. Anal. At. Spectrom. **24**, 602–604 (2009).

71. A. M. Popov, F. Colao, and R. Fantoni, "Spatial confinement of laser-induced plasma to enhance LIBS sensitivity for trace elements determination in soils," J. Anal. At. Spectrom. **25**, 837–848 (2010).

72. M.-H. L. Yong-Zeng Lin, Ming-Yin Yao, Tian-Bing Chen, Wen-Bing Li, Mei-Lan Zheng, Xue-Hong Xu, Jian-Ping Tu, "Analysis of Cr in soil by LIBS based on conical spatial confinement of plasma," Guang pu **33**, 3120–3 (2013).

73. L. Schlessinger and J. A. Wright, "Inverse-bremsstrahlnng absorption rate in an intense laser field," Phys. Rev. A **22**, 909–915 (1980).

74. K. N. Leung, T. K. Samec, and A. Lamm, "Optimization of permanent magnet plasma confinement," Phys. Lett. A **51**, 490–492 (1975).

75. S. S. Harilal, M. S. Tillack, B. O'Shay, C. V. Bindhu, and F. Najmabadu,

"Confinement and dynamics of laser-produced plasma expanding across a transverse magnetic field," Phys. Rev. E - Stat. Nonlinear, Soft Matter Phys. **69**, 1–11 (2004).

76. J. D. Huba, A. B. Hassam, and D. Winske, "Stability of sub-Alfvénic plasma expansions," Phys. Fluids B **2**, 1676–1697 (1990).

77. X. K. Shen, Y. F. Lu, T. Gebre, H. Ling, and Y. X. Han, "Optical emission in magnetically confined laser-induced breakdown spectroscopy," J. Appl. Phys. **100**, (2006).

78. A. Hussain, Q. Li, Z. Hao, X. Gao, and J. Lin, "The effect of an external magnetic field on the plume expansion dynamics of laser-induced aluminum plasma," Plasma Sci. Technol. **17**, 693–698 (2015).

79. NobelPrize.org, "The Nobel Prize in Physics 1970," https://www.nobelprize.org/prizes/physics/1970/summary/.

80. F. P. Bowden and D. Tabor, "Existence of Electromagnetic-Hyrodynamic Waves," Nat. Publ. Gr. (1942).

81. V. N. Rai, H. Zhang, F. Y. Yueh, J. P. Singh, and A. Kumar, "Effect of steady magnetic field on laser-induced breakdown spectroscopy," Appl. Opt. **42**, 3662 (2003).

82. C. Nygren, "Phone Call 10 Dec 2020," (2020).

83. E. J. Judge, J. E. Barefield, J. M. Berg, S. M. Clegg, G. J. Havrilla, V. M. Montoya, L. A. Le, and L. N. Lopez, "Laser-induced breakdown spectroscopy measurements of uranium and thorium powders and uranium ore," Spectrochim. Acta - Part B At. Spectrosc. **83**–**84**, 28–36 (2013).

84. D. Meeker, "Finite Element Method Magnetics," https://sourceforge.net/projects/femm/.

85. M. H. Ebinger, M. L. Norfleet, D. D. Breshears, D. A. Cremers, M. J. Ferris, P. J. Unkefer, M. S. Lamb, K. L. Goddard, and C. W. Meyer, "Extending the Applicability of Laser-Induced Breakdown Spectroscopy for Total Soil Carbon Measurement," Science (80-.). **67**, 2001–2004 (2002).

86. M. B. Shattan, D. J. Miller, M. T. Cook, A. C. Stowe, J. D. Auxier, C. Parigger, and H. L. Hall, "Detection of uranyl fluoride and sand surface contamination on metal substrates by hand-held laser-induced breakdown spectroscopy," Appl. Opt. **56**, 9868 (2017).

87. "Nuclear Power," https://www.nuclear-power.net/nuclear-power-plant/nuclear-fuel/thorium-vs-uranium/#:~:text=Thorium is a naturally-occurring element and it is,phosphate mineral). Thorium has 6 naturally occurring isotopes.

88. N. Idris, K. Lahna, Fadhli, and M. Ramli, "Study on Emission Spectral Lines of Iron, Fe in Laser-Induced Breakdown Spectroscopy (LIBS) on Soil Samples," J.

Phys. Conf. Ser. **846**, (2017).

89. J. D. Auxier, "Email correspondence 11Dec2020," (2020).

90. "Quantel Laser," https://www.quantel-laser.com/home.html.

91. Y. Liu, L. Gigant, M. Baudelet, and M. Richardson, "Correlation between laser-induced breakdown spectroscopy signal and moisture content," Spectrochim. Acta - Part B At. Spectrosc. **73**, 71–74 (2012).

92. H. Sobral and A. Robledo-Martinez, "Signal enhancement in laser-induced breakdown spectroscopy using fast square-pulse discharges," Spectrochim. Acta - Part B At. Spectrosc. **124**, 67–73 (2016).

93. G. C. Y. Chan, I. Choi, X. Mao, V. Zorba, O. P. Lam, D. K. Shuh, and R. E. Russo, "Isotopic determination of uranium in soil by laser induced breakdown spectroscopy," Spectrochim. Acta - Part B At. Spectrosc. **122**, 31–39 (2016).

94. R. Bro and A. K. Smilde, "Principal component analysis," Anal. Methods **6**, 2812–2831 (2014).

95. J. Shlens, "Shlens2006_PCATutorial," Measurement 1–13 (2005).

96. J. Goldstein, D. E. Newbury, D. C. Joy, C. E. Lyman, P. Echlin, E. Lifshin, L. Sawyer, and J. R. Michael, *Scanning Electron Microscopy and X-Ray Microanalysis*, 3rd Editio (Springer US, 2003).

REPORT DOCUMENTATION PAGE

Form Approved OMB No. 0704-0188

1. REPORT DATE (DD-MM-YYYY)	2. REPORT TYPE	3. DATES COVERED (From - To)
03/25/2021	Master's Thesis	SEP 18 - SEP 21

4. TITLE AND SUBTITLE
Development of a magnetic confinement attachment for enhanced signal in handheld laser induced breakdown spectroscopy soil analysis.

5a. CONTRACT NUMBER
5b. GRANT NUMBER
5c. PROGRAM ELEMENT NUMBER

6. AUTHOR(S)
LTC Alfred C. Anderson

5d. PROJECT NUMBER
5e. TASK NUMBER
5f. WORK UNIT NUMBER

7. PERFORMING ORGANIZATION NAME(S) AND ADDRESS(ES)
Air Force Institute of Technology
Graduate School of Engineering and Management (AFIT/EN)
2950 Hobson Way
Wright-Patterson AFB OH 45433-7765

8. PERFORMING ORGANIZATION REPORT NUMBER
AFIT-ENP-MS-21-D-016

9. SPONSORING/MONITORING AGENCY NAME(S) AND ADDRESS(ES)
Intentionally Left Blank

10. SPONSOR/MONITOR'S ACRONYM(S)
11. SPONSOR/MONITOR'S REPORT NUMBER(S)

12. DISTRIBUTION/AVAILABILITY STATEMENT
Distribution Statement A
Approved For Public Release; Distribution Unlimited

13. SUPPLEMENTARY NOTES

14. ABSTRACT
Field techniques for characterizing low levels of heavy elements of less than 100 parts per million in soils tend to be unreliable because of the relatively weak signal of these elements and the large, variable background inherent to analyzing soils with minimal sample preparation. To enhance the detection and analysis capability of a handheld laser-induced breakdown spectroscopy (LIBS) instrument, this work investigates the effects of a unique magnetic confinement apparatus on signal intensities, focusing on five iron lines as well as those from actinides in 11 soil samples. The proposed magnetic confinement apparatus achieved over 0.8 T but did not amplified the elements' peak intensities of the samples equally.

15. SUBJECT TERMS
Handheld LIBS, Magnetic Confinement, Principal Component Analysis, Trace Elements, Actinides

16. SECURITY CLASSIFICATION OF:			17. LIMITATION OF ABSTRACT	18. NUMBER OF PAGES	19a. NAME OF RESPONSIBLE PERSON
a. REPORT	b. ABSTRACT	c. THIS PAGE			LTC Michael B. Shattan, AFIT/ENP
U	U	U	UU	80	19b. TELEPHONE NUMBER (Include area code) 937-255-3636 x 4587 michael.shattan@afit.edu

Standard Form 298 (Rev. 8/98)
Prescribed by ANSI Std. Z39.18